QATAR UNIVERSITY

COLLEGE OF ENGINEERING

ASSESSMENT OF TURBULENCE MODELS FOR HYDROFRACTURING SLURRY TRANSPORT SIMULATION IN HORIZONTAL PERFORATED PIPE

BY

MOHAMED KHAIRY MOHAMED YOUSSEF

A Thesis Submitted to

the College of Engineering

in Partial Fulfillment of the Requirements for the Degree of

Masters of Science in Mechanical Engineering

June 2020

© 2020. Mohamed Youssef. All Rights Reserved.

COMMITTEE PAGE

The members of the Committee approve the Thesis of
Mohamed Youssef defended on 19/08/2020.

_____

Dr. Saud Ghani
Thesis/Dissertation Supervisor

Approved:

_____

Khalid Kamal Naji, Dean, College of Engineering

ABSTRACT

YOUSSEF, MOHAMED, K., Masters : June : 2020, Masters of Science in Mechanical Engineering

Title: Assessment of Turbulence Models for Hydraulic Fracturing Slurry Transport Simulation in Horizontal Perforated Pipe.

Supervisor of Thesis: Saud, A., Ghani.

Hydraulic fracture is a well stimulation process that involves injecting pressurized liquid at high velocity to initiate and propagate a fracture in the deep rock formations through which hydrocarbons are extracted [1]. Typically, the pressurized liquid, or the fracking liquid, is water mixed with sand. The water creates the fracture and the sand maintains the void open. Hydraulic fracture stimulation is a standard completion process for modern unconventional gas reservoirs. Proppant transport through the wellbore is a major consideration when a horizontal well is fractured.

CFD simulation is utilized to understand the hydrofracturing process. This study is characterizing different turbulence models that can capture the hydraulic fracturing process. Selection of a suitable CFD turbulence model is carried through investigating slurry flow in a horizontal pipe and employing various turbulence models. The CFD results obtained from a Standard k-ε, Renormalization Group (RNG) k-ε and Reynold-Stress-Model (RSM) were assessed. The (RNG) k-ε model deemed the best turbulence model when capturing the slurry flow behavior.

In a laboratory experiment, particle image velocimetry (PIV) was used to non-intrusively measure the transportation of sand slurry flow in a horizontal see through pipeline with perforated holes. The investigation reports the results of the slurry flow

patterns, the slurry flow pressure drop, the concentration profile and velocity distribution at the perforated holes.

The experimental results supported the validity of the (RNG) k-ε model in obtaining reliable predictions of the slurry flow. A linear relationship between the surly velocity and the sand solid phase velocity was established.

Keywords: Horizontal well stimulation, Hydraulic fracturing; Slurry transport; CFD, Turbulence models.

DEDICATION

I dedicate this work to Dr. Saud Ghani and my professors in the mechanical engineering department for their faithful support and guidance during the completion of this thesis.

ACKNOWLEDGMENTS

First and foremost, I would like to praise God Almighty and thank him for giving me this opportunity to be among distinguished professors and outstanding students and complete my academic thesis for postgraduate studies from Qatar University.

I would like to express the deepest appreciation to my advising Dr. Saud Ghani for his support, guidance, valuable comments, encouragement, and positive attitude during the execution of the thesis. My appreciation also extends to my colleague Eng. Ahmed Osama and Eng. Suliman who helped me in performing the experimental works.

Finally, I am highly indebted to my mother, father, and siblings, who supported me spiritually through my life and sustain a positive atmosphere in which to do science.

TABLE OF CONTENTS

LIST OF TABLES

LIST OF FIGURES

ABBREVIATIONS AND ACRONYMS

RNG	Renormalization Group	$\bar{\bar{\tau}}_s$	stress-strain tensors of the solid phase
RSM	Reynold-Stress-Model	$\vec{g}$	Gravitational acceleration
PIV	particle image velocimetry	K_{fs}	inter-phase drag force coefficient
EIA	energy information administration	$\vec{F}_{lift}$	lift force
D	horizontal pipe diameter	C_{vm}	virtual mass coefficient
$\boldsymbol{v}$	Slurry velocity	μ_q	Shear viscosity of phase q
CFD	Computational Fluid Dynamics	λ_q	bulk viscosity of phase q
$\boldsymbol{\alpha_q}$	volume fractions of phase q	$\bar{\bar{I}}$	identity tensor
$\boldsymbol{\alpha_f}$	Volume fraction of fluid	k	Turbulence kinetic energy
$\boldsymbol{\alpha_s}$	Volume fraction of solid	ε	turbulence dissipation rate
V	space occupied by each phase	u_i	velocity component in corresponding direction
$\boldsymbol{\rho_q}$	effective density of the slurry flow	G_k	generation of turbulence kinetic energy due to the mean velocity gradients
$\boldsymbol{\rho_q}$	physical density of phase q	G_b	generation of turbulence kinetic energy due to buoyancy.
$\overrightarrow{\boldsymbol{v_q}}$	velocity vector of phase q	σ_k	turbulent Prandtl numbers for k

$\vec{v}_f$	velocity vector of fluid	σ_ε	turbulent Prandtl numbers for ε
$\vec{v}_s$	velocity vector of solid	$\sigma_k, \sigma_\varepsilon,$	Adjustable constants of
∇P	static pressure gradient	$C_{1\varepsilon},$	turbulence model in which
∇P_s	solid pressure gradient	$C_{2\varepsilon},$	they have been arrived by
$\nabla.\bar{\bar{\tau}}$	viscous forces	$C_{3\varepsilon},$	numerous iterations of data
$\bar{\bar{\tau}}_f$	stress-strain tensors of the fluid phase	$C_\mu, \eta_0,$ β	fitting for a wide range of turbulent flows.

CHAPTER 1: INTRODUCTION

1.1 Introduction on hydrofracturing treatment

Hydraulic fracturing has played a significant role in increasing the production of oil and gas wells [1-2]. According to the energy information administration (EIA), 69% of all oil and natural gas wells drilled in the United States are hydraulically fractured [3]. It is of potential importance in various oil and gas companies in Qatar such as Total Company. After the well is drilled, the hydrocarbon is derived to the wellbore through existing flow channels in several ways such as natural or artificial fluid displacement, fluid expansion, capillary expulsion, gravity drainage, and compaction of sediments and rocks. Multiple techniques can be applied independently or simultaneously to displace the oil and gas to the wellbore. Wells production rate could be commercially insufficient due to two main reasons. Namely, low formation permeability, which prevents the hydrocarbons to drain into the wellbore at a sufficiently high rate, or wellbore damage sustained during the drilling process [4].

In hydraulic fracturing, fluid is injected until the pressure of the fluid overcomes the inherent stresses of the rock or is greater than the forces holding the rock together. Eventually, the rock splits apart, forming a fracture [5]. In order to hold the fracture open, fracturing fluid or the slurry flow must be pumped into the fracture rapidly to allow the propping agent (sand) carried by the fluid to enter the fracture and hold the walls of the fracture apart (Figure 1). Hence, fracture crack expands around the wellbore and new and larger flow channels are created out into the undamaged portions of the reservoir and may also connect the preexisting natural fractures and micro-fractures (fissures) to the wellbore. if the propping agent is not used, the fracture walls can heal or close [7-9].

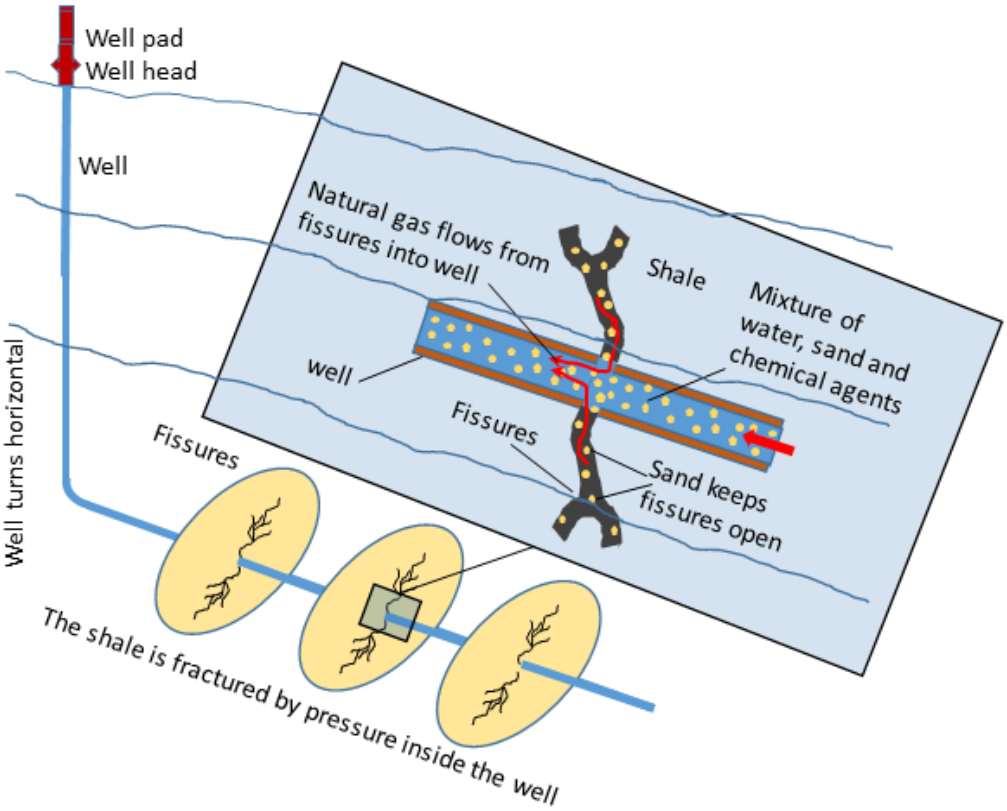

Figure 1. Hydrofracturing in horizontal well [5, 6].

1.2 Background of fracturing

The essential idea of fracturing almost started in 1857, when Preston Barmore used gunpowder in the well to fracture the rock and increase the gas flow production [10-11]. In 1866, US patent was issued by Edward Robert who developed an invention with the title of "Improvement In Method of Increasing Capacity of Oil-Wells" in which the wellbore is filled with water to dampen the explosion and prevent any debris blowing back up the hole and amplify its effects. He also developed a nitro-glycerine 'torpedo', replacing the gunpowder that had previously been used [12-13]. In the 1940s, Floyd Farris of Stanolind Oil studied the relation between observed well performance and treatment pressure "formation breakdown" during fracturing by acidizing, injecting water, and filling with cement [14-15]. After 1950, well

stimulation with high explosive gunpowder became less common because the oil industry found that commercial fracturing treatments could achieve the same results. Whereas, the use of explosives was limited by the severe risks associated with handling unstable materials [4].

The first attempts to hydrofrac a well was performed in the Klepper gas well, Hugoton gas field in 1947. This well was completed and produced gas from four limestone horizons between 2340 and 2580 ft. The treatment of the well was done using a centrifugal pump for mixing the gasoline-base napalm gel fracturing fluid, then the fluid was injected with a high-pressure positive-displacement pump into the wellbore. However, the production rate of gas from these zones did not significantly improve and it was considered as an unsuccessful attempt to stimulate the well [4][16].

In 1949, Hydrofrac process was introduced more widely to the industry in a paper by Clark of the Stanolind Oil and Gas Company. Clark stated that the process consists of two steps:

1- Injecting a high-pressure viscous liquid containing a propping agent such as sand in order to fracture the formation.
2- Changing the viscosity of the liquid from high to low so that the liquid will flow back out of the well and not stay in place and plug the crack which it has formed.

One of the requirements must be met with considering these two steps is the hydraulic fluid should carry in suspension a propping agent such as sand so that once a fracture is formed, the sand will prevent the fracture from closing off and the fracture will remain to serve as a flow channel for gas and oil. Secondly, the ideal fluid should be an oily one rather than a water-based fluid, to avoid decreasing the permeability of the formation to oil or gas. However, he predicted that future work

with this process may indicate that it is more economical to use a water base for the hydraulic fracturing fluids than the more expensive gasoline and crude oil base fluids, particularly in formations not appreciably contaminated with argillaceous materials [17].

After the mid of 19th century, the technology and knowledge of fracturing have developed with time. Halliburton started to use treatments composed of injecting small volumes of fluid (200-400 gal) mixed with sand (0.5 lb/gal), injected at rates from 2 to 4 bbl/min. While operators experimented with a higher injection rate, larger production was observed. Progressively, the job sizes and the injection rates began to increase. In late 1952, the treatment of wells became more cost-effective and efficient and the treatment trend curve has risen steadily since then on average of 1.1 lb/gal for sand/fluid ratio [4].

1.3 General procedures for successful stimulation treatment

The variables that affect the stimulation process, could impose some limitations on the operating procedures for example the volume of proppant and the pumping flow rate during the hydrofracturing treatment may be limited due to the wellbore dimensions which can cause excessive pressure-drop at high proppant concentration and high flow rates [9]. Review of past hydraulic fracture treatments indicates that insufficient volume of proppant and incorrect selection of proppant can cause the failure of stimulation treatment while in the case of successful treatment the following common procedures must be observed [4]:

(1) The fracturing fluid is mainly water base, (2) Spacers is used to help reduce proppant concentration and, thus, reduce the possibility of a screen-out, (3) reducing pumping rates near the end of the treatment to enhance proppant packing and fracture conductivity, (4) using proppant agents having chemical stability, high strength, and

high permeability retention under loading.

The availability and low unit cost of sand have made sand the most popular of all propping materials. Sand is brittle and tends to crush under heavy loads. Figure 2 illustrates the relation between permeability and mean proppant diameter at 2000 Psi closure stress. A direct linear relationship between mean proppant diameter and permeability exists, where, as the mean proppant diameter increases, the permeability of the well increases as well [4].

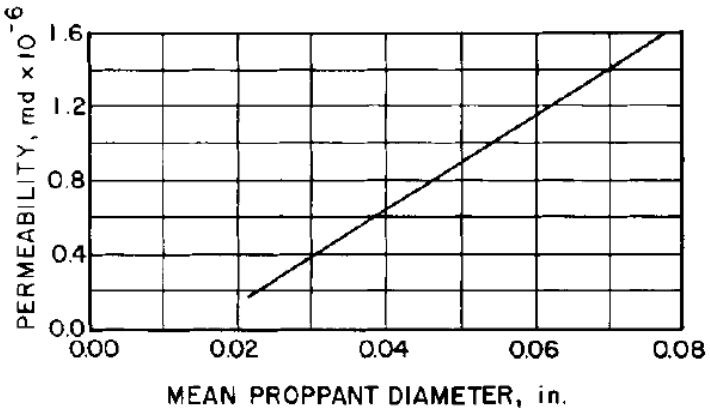

Figure 2. Permeability in millidarcy verse the mean propant diameter in inch [4]

1.4 Scope and aims of the work

This research is focusing on the transportation of sand particles in a flowing water medium within an annular pipe up to the perforated gun holes. The thesis investigates the pressure drop between the pipe inlet and the perforated holes at different slurry velocities, at different sand particles average concentrations for the outlet gun holes, and the velocity correlation of sand particles between the inlet port and the outlet holes. The aim is to present a better understanding of the principles that

affect the design of slurry systems in horizontal pipelines.

This research presents previous relevant experimental and numerical investigations on slurry flows. Hence, introducing the experimental setup and the numerical methods used. Characterization of the CFD turbulence models and the validation of the selected turbulence model is discussed. The results are presented in terms of the pressure gradient, particle concentration and velocity distribution off the gun holes.

1.5 Research Objectives

The overall goals of this thesis are:

1. Characterizing turbulence models that can capture the hydraulic fracturing slurry flow behavior in a horizontal pipe.
2. Investigating the pressure drop between the pipe inlet and perforated holes at different slurry velocities.
3. Investigating the sand average concentrations of the different outlet perforated holes at different slurry velocities.
4. Investigating the velocity correlation of sand particles between the inlet and the outlet holes.

Accordingly, achieving these overall goals require fulfillment of three sub-objectives:

1. Characterizing the process of hydrofracturing treatment, identifying the fluid and proppant agent which have been used in this process over the years, and analyzing the challenges and difficulties in the hydrofracturing process.
2. Classifying the slurry rheology and flow regimes.
3. Investigating the previous works in literature which studied and contributed to the field of slurry flow in horizontal well experimentally and numerically.

CHAPTER 2: LITERATURE REVIEW

2.1 Introduction on slurry flow

A semi-liquid mixture of solid particles with a carrier liquid is known as Slurry. Overall, sand is useful to easily prop open the fractures in shallow formations. It is because sand doesn't cost much per pound as compared to other proppant i.e. silica sand, ceramic proppants, and resin-coated sand (RCS). While, the solid particles are merely just sand. Similarly, there are various kinds of liquid carriers. However, water is the practical liquid that is used in the thesis unless otherwise stated. These slurries can also be called conveying or hydraulic transport, if they are used for the transportation of some material that is suspended in water [18].

To understand the whole slurry flow process, it is essential to have an accurate prediction of slurry flow characteristics. The characterization of the slurry flow regime is useful in developing and validating empirical and numerical multiphase models. In industry, it is very important to define the type of slurry flow regimes for designing, optimization, and controlling processes involving slurry flow. In spite of the large area of application, a complete description of the flow based only on differential equations is not possible, due to the complexity of two-phase flow systems. Many researchers studied over the years the effect of solid particle concentrations, pressure drop, and velocity distribution along with other flow parameters to understand the flow regime governing mechanisms [9, 19]. Generally, the attempt to solve the slurry flow regimes problems could be approached by begins from experimental data and simplifies know correlations for some parameters by dimensional analysis. The second method is using numerical methods to solve the basic equation of motion with mathematical assumptions for different terms. Computational Fluid Dynamics (CFD) is a computer-based numerical analysis system

[20]. This sophisticated CFD develops and adopts suitable mathematical models in order to provide a tool for the analysis of complex solid-liquid slurry flow problems. With lower cost and great ease, CFD helps researchers to conduct detailed numerical analysis of the complex flow regime. CFD provides information within the computational domain, extensively regarding the variation locally made, of the flow parameters [19]. This chapter describes slurry rheology and its associated characteristics, flow regimes, and previous experimental and numerical studies related to the slurry flow in a horizontal pipeline.

2.2 Rheology of the slurry

Rheology is one of the most important characteristics associated with slurries. It can be defined as the study of the behavior of materials related to their flow, for both fluids and solids. This definition can easily be applied to complex microstructural substances which may include mud, suspensions, slurries, and sludge. Trying to understand the rheology related to slurries is very basic and necessary in order to properly design and engineer slurry systems [21, 22]. The same rheology is as well, a property that is dynamically concerned with the microstructure that is the basis of the slurry. It is henceforth, easily affected by different attributes e.g. the shape, density, mass fraction, and size of the solid suspended particles. A similar effect is imparted by the viscosity and density of the carrier liquid. Therefore, this section will give an outline to all the basic qualities of slurry flows. It will also explain the key physical properties of slurries. Accurate engineering and efficient designing are dependent on these properties.

2.2.1 Newton's Law of viscosity

Viscosity is that one rheological attributes which has a lot of significance when it comes to liquids. Simultaneously, viscosity can be known as the quantity that

shows any fluid's ability to resist flow. It is imparted with friction forces in between the particles prevents them from moving in conjunction to one and another. The idealized situation used to describe viscosity is Couette flow. It is the phenomenon that involves the trapping of a fluid in between a horizontal plate simultaneously moving at a constant speed V_0 and a stationary plate horizontally, across the surface of the liquid. In turn, the topmost layer of the liquid will start moving parallelly to the moving plate, this will take place at the exact speed as the moving plate ($V = V_0$). Therefore, every layer of the liquid will start to move slower as compared to the layer on the top of it because of the frictional forces that are resisting the relative motion. Furthermore, the fluid will start to exert a force opposite to the direction of its motion, on the moving top plate. Therefore, a force externally, will be required in order to move the top plate [23]. The Couette flow is exemplified in figure 3.

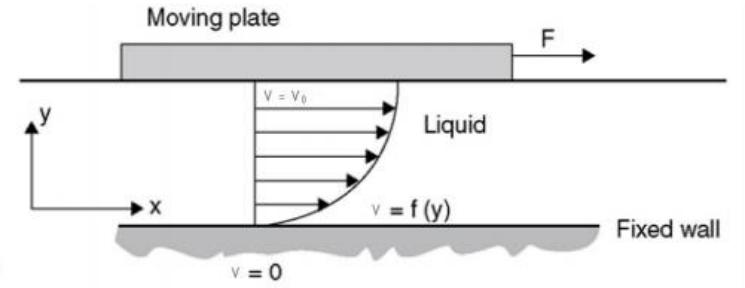

Figure 3. Couette flow for defining viscosity [24].

The external force of friction F will be proportional to speed V_o as well as the area A of the plates, and at the same time, inversely being proportional to their separation. It is shown in the equation (1).

$$F = \mu A \frac{\partial V}{\partial y} \quad \ldots (1)$$

Where:

μ: Fluid dynamics viscosity.

A: surface area

V_0: moving plate speed

Y: Separation of the plates on the y-axis

A fluid having a viscosity that is not dependent on the stress is known as a Newtonian fluid (kept after the great name of Isaac Newton); he showed the viscous forces with the usage of the differential equation (2). For a Newtonian fluid, the shear stress at a surface element parallel to a flat plate at the point y is given by:

$$\tau = \mu \frac{\partial V}{\partial y} \quad \ldots (2)$$

Where:

V: The flow velocity along the boundary;

y: The height above the boundary.

Pa·s is the SI unit for viscosity. However, viscosity can be also presented in centipoises, (cP). Similarly, the shear stress comes in direct proportion to the velocity gradient (the shear rate), for Newtonian fluids. In Addition, shear stress will be given off as zero if velocity gradient is also zero.

2.2.2 Slurry density

Density of slurry is influenced by, the concentration of solid particles, the density of the carrier liquid and density of the solid particles. For the concentration of the solid particles, moreover, the value is often shown in percent by weight. The only reason to it is convenience; when the calculation is done for the pipeline throughout

tonnages. Despite that, slurry properties in pipeline flow are influenced greatly by the volume of solids. Similarly, density of slurry using solid percent by weight can be defined easily by the following equation (3) [25].

$$\rho_m = \frac{100}{\frac{c_w}{\rho_s} + \frac{100 - c_w}{\rho_l}} \quad \ldots (3)$$

Where

ρ_m *= density of slurry (kg/m^3)*

c_w *= concentration of solids by weight in the slurry (%)*

ρ_s *= density of the solids (kg/m^3)*

ρ_l *= density of liquid without solids (kg/m^3).*

The concentration of solids by volume, CV, is expressed in percent by the following equation (4) [25]:

$$C_V = \frac{C_w \rho_m}{\rho_s} = \frac{100 \frac{C_w}{\rho_s}}{\frac{C_w}{\rho_s} + \frac{100 - C_w}{\rho_l}} \quad \ldots (4)$$

The concentration by weight of solids, CW, is conversely expressed, in percent by the equation (5) [25].

$$C_W = \frac{C_v \rho_s}{\rho_m} = \frac{\frac{C_v}{\rho_s}}{C_v \rho_s + (100 - C_v)} \quad \ldots (5)$$

Slurry density is measurable directly by using online measurements or in laboratory testing. However, when settling slurries are being measured, care is required for the assurance of keeping the larger particles from settling out before the

measurement is done. Similarly, flow rates have to be suitably increased to assure appropriate suspension of the particles in the case of online measuring. It is possibly better to sometimes, make measurements of the fluid and particle densities in order to provide a definition of the density of the slurry with a provided concentration. In contrast to it, slurry density is usable as a measure of concentration [26].

2.3 Fluid Flow Regimes

In general slurry flow regimes can be classified into four principal regimes in horizontal pipe according to the solid concentration profile; homogeneous, heterogeneous, stationary bed and moving bed. When systems of slurries are being designed, possibly the most influential part that requires prior determination is the behavior of settlement that is being imparted the slurry. So, slurries are, further divided into two types, in practice, basing on the settlement of particles inside the carrier liquid in the given flow conditions. Solid particles normally settle in all sorts of carrier liquid when provided with enough time. Similarly, all the methods for gravity separation are centered on the same fact. So, when applied practically, it is very crucial to know the behavior of the solid particles when the sole objective is the transportation of the solid particles by the use of hydraulic conveying, i.e. slurry pumping [26].

In settling or heterogeneous slurries, the particles do not get suspended properly in the carrier liquid. Instead, simply transport with the liquid. Contrary to this, they become suspended by turbulence at high velocities. With heterogeneous slurries, it is necessary to take care to prevent plugging of pipelines, so that keeping the velocities of the pipelines higher than the critical settling velocity is possible, that comes with the particles. A Heterogeneous slurry is usually water based and comes with a huge quantity of solid particles that are greater than 100 μm in size. At the

same time, a lesser content of solids that are smaller than 40 μm (fines) means that the fine particles and water (carrier fluid) is somewhat same as water. Non-settling or homogeneous slurries are those which have solid particles being in a suspended state in the carrier liquid in a continuous phase. The homogeneous slurries have features that may or may not vary significantly from different basic Newtonian liquids or water. The finer particles henceforth, make an increment in the viscosity of fluid [26]. In general, settling slurries are more complex and have a significant effect on pump performance, as a result, many practical applications tend to use non-settling slurry.

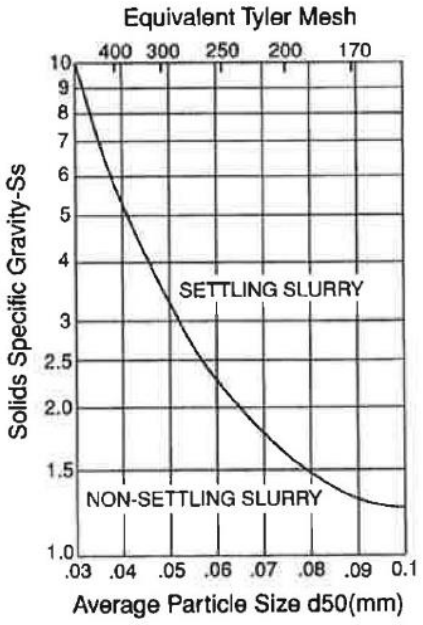

Figure 4. comparatively harsh method to find the slurry is settling or non-settling [27]

Whether the slurries are non-settling or settling, is decided by the specific gravity and the particle size of solid particles. Therefore, a raw determination can be estimated between non-settling and settling behavior using a chart given in the Figure

4 [27]. This is a comparatively harsh method and therefore, should be treated as such. Moreover, it only considers the specific gravity and the average particle size of the solid, however it is to be noted that slurry concentration also effects on the settling behavior of solids.

2.3.1 Transitional velocities

Slurry flow in a horizontal pipe can be classified with solid phase concentration into four distinct flow regimes; Stationary bed, moving bed, asymmetric flow and symmetric flow (Figure 5). The Pressure drop per meter of pipe are on the plot against the mean flow velocity. So, the pressure drop behavior of every flow regime differs greatly.

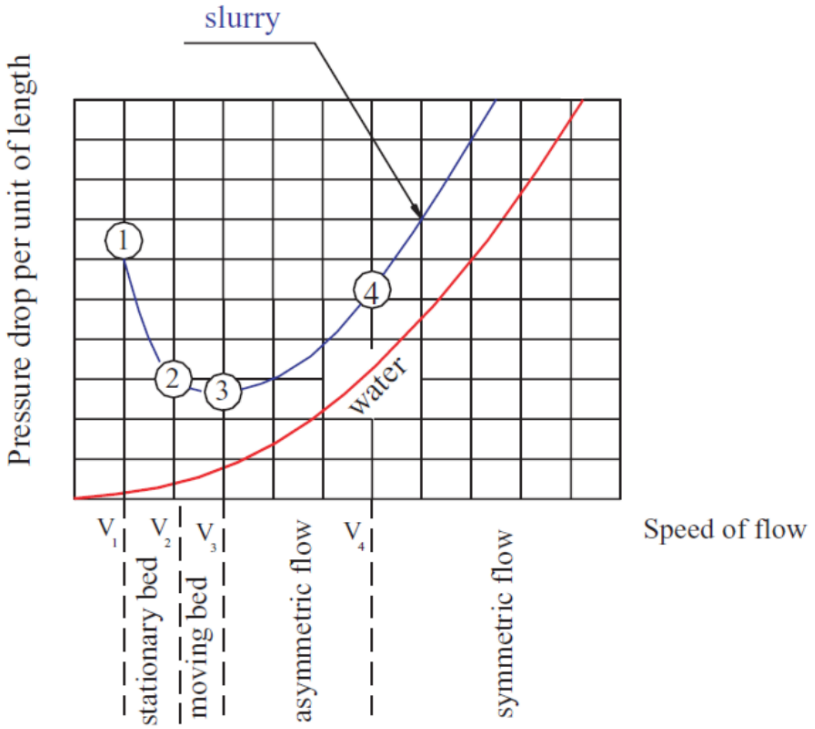

Figure 5. Pressure drop vs the mean flow velocity at different flow regimes of heterogenous slurries [26].

As the heterogeneous slurry velocity decreases, the solids-concentration gradient increases until either a stationary or a slowly moving particle bed appears along the pipe bottom. That the lowest pressure drop is achieved at transitional velocity of which a particle bed forms, is defined as the critical velocity, deposition velocity or limiting velocity (V_3) and represents the lower pump rate limit for minimum particle settling. A further decrease in slurry velocity increases pressure loss, as indicated by the characteristic upward hook of slurry curve, and may also cause pipe plugging. The motion of solid particles starts in the upper pipe as the speed of the slurry exceeds the moving bed, where gravity causes asymmetrical suspension configuration of forces and segregation is always present. At extremely high velocity, fine particle sized, and or small density differences between solids and liquid, a symmetrical suspension is formed in which the solid are uniformly distributed through the liquid. Later, hydraulic fracturing slurries are shown to exhibit this heterogeneous response.

2.3.2 Laminar and turbulent models

In respect with driving forces, fluid flow is categorized into two different types; laminar flow and turbulent flow (Figure 6) [28]. Laminar Flow: A fluid flows through a smooth path with no disruption between its infinitesimal parallel layers. It is quite compatible to examine laminar flow both numerically and experimentally. On the other hand, turbulent flow is a type of fluid flow that is unsteady, enormously irregular in space and time, three-dimensional, rotational, dissipative (in terms of energy), and diffusive (transport phenomenon) at high Reynolds numbers. Due to those divergences in turbulent flow, extremely small-scale fluctuations emerge in velocity, pressure, and temperature. Thus, requires rigorous effort during experimental and numerical examinations [29].

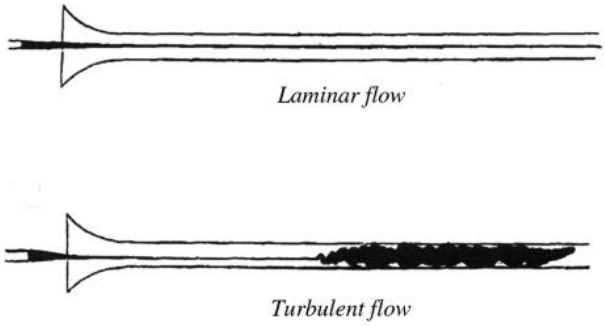

Figure 6. Turbulent and laminar flow [23].

Earlier, it was difficult to perceive the type of fluid flow numerically. Irish scientist Osborne Reynolds (1883) discovered the dimensionless number that predicts fluid flow based on static and dynamic properties such as density, velocity, length, and dynamic viscosity [28]:

$$\text{Re} = (\text{inertial force}) / (\text{viscous force})$$

$$= \frac{\rho V L}{\mu} \qquad \ldots (6)$$

Where ρ (kg/m^3) is the density of the fluid, V (m/s^2) is the characteristic velocity of the flow, L (m) is the characteristic length scale of flow, and μ (Pa*s) is the dynamic viscosity of the fluid. Figure 7 explains the type of the flow based on his Reynolds number.

Type	Flow type	Reynolds Number
Internal	Laminar regime	up to Re=2300
	Transition regime	2300<Re<4000
	Turbulent regime	Re>4000
External	Laminar to Turbulence	$Re>3\times10^5$

Figure 7. Types of the flow according to the Reynolds number

2.3.3 Calculation of critical deposition velocities

That velocities in which the lowest pressure drops achieved is at flow transforming from moving bed to asymmetric flow is called the critical deposition velocities (V_D). Also, this transition point has different names as critical velocity or limiting velocity. The initial equation for the determination of the V_3 (or V_D) transitional velocity is given in 1952 by Condolios and Durand [30], it is shown in the equation (6):

$$V_D = F_L\sqrt{2gD_i[\rho_s - \rho_L)/\rho_L]} \quad \dots (7)$$

The Durand factor is shown mostly in a graph of single of thin-graded particles. Simultaneously, basing on the work done by Durand (1953), the original graph, is normally thought of to be a bit conservative for a lot of slurries that include a mix of particles of various sizes. But, it is still used, e.g. Weir, which is a supplier of pumps that specializes in slurry pumps [31]. Furthermore, the Durand's limiting settling velocity parameter diagram for narrow graded particles is also given in

appendix A [32]. Moreover, Weir consider narrow particle size distribution as one where the ratio of particles sizes, does not exceed approximately 2:1 expressed as testing screen apertures, for about 90 % by weight of the total solids.

Therefore, several other correlations were proposed as an experimental factor, each of which attempted for the improvement in the pioneering work given by Durand. The reviews of different correlations are accessible in literature, for example by Turing *et al*. (1987) and Carleton & Cheng (1974) [33]. A modified Durand's limiting settling velocity parameter diagram, suitable for a more widely graded particle sizes, later used by Weir (Anon, 2009) is shown in the Appendix B [32].

In 1991, Schiller and Herbich proposed the equation (7) to calculate the Durand factor:

$$F_L = \{(1.3 \times C_v^{0.125})[1 - \exp(-6.9 \times d_{50})]\} \quad \ldots (8)$$

Where:

C_v: volumetric concentration in percent

d_{50}: Average diameter of solid particles (mm)

In 1970, Wasp and Aude, later created an equation that was modified, the basis of it was laid on the equation given by Durand and Condolios (equation 6), known as Wasp's equation. There was an included ratio between the inner diameter of the pipe and the solid particle diameter. Therefore, the equation also comprises of a modified Durand factor, F_L'. Wasp's equation is given in equation (8).

$$V_D = F_L' \sqrt{2gD_i[\rho_s - \rho_L)/\rho_L]} \left(\frac{d_{50}}{D_i}\right)^{1/6} \quad \ldots (9)$$

Where:

$$F_L' = 3.399 \times C_V^{0.2156} \quad \ldots (10)$$

The results for critical deposition velocity, coming from Wasp's equation are naturally lower than those given off by original Durand formula. Later in 2006, Wilson et al. use a comparable term, it was based on the work done by Wilson's earlier in the 1970's, the velocity at limit of stationary deposition. This can be called a flow speed, in the base of which there is a formation of a stationary bed inside the pipe. After that, they paralleled this with the critical deposition velocity by Durand. Contrary to this, the comparison is not completely accurate. So, the critical deposition velocity shows a flow speed that has a moving bed forming below it, in Durand's model. As mentioned earlier, there is a noticeable difference between a stationary bed and a moving bed [34].

Wilson et al. (2006) concluded that the velocity is concentration dependent at the extent of stationary deposition, that have low values at likewise concentrations which simultaneously rise to the highest value at an intermediate concentration value, soon after this, dropping off again at concentrations that are much higher. They made use of a force balance analysis for the development of a model to predict, at the extent of stationary deposition, the velocities, and specifically for the highest velocity (denoted VSM). The problem that arose with the model is, it requires too much values that are not accessible for a process engineer when considering the basic engineering timing of a project. Moreover, it needs a lot of values that are solely published as graphs. This makes the usage weighty, as there are needs when the sizing has to be done for hundreds of different pumps and pipelines.

2.4 Previous work on slurry flow:

Researchers investigated numerically and experimentally, the solid-liquid slurry flow through both vertical and horizontal pipelines. For a better understanding of the slurry flow process, the researchers developed general numerical models for the description of the characteristics regarding various flow parameters which includes, concentration distributions, pressure drops, deposition velocity distributions.

Using a diffusion model, initial studies of O'Brien (1933), and Rouse (1937) were able to predict the concentration distribution inside a gravity based open channel slurry flow that contained extremely low solid volumetric concentration [34-36]. Following this, other researchers Shook and Daniel (1965) Karabelas (1977), Shook et al. (1968), Gillies et al. (1991), Roco and Shook (1983), Gillies and Shook (1994), Seshadri et al. (1982), Roco and Shook (1984), Gillies et al. (1999), Gillies and Shook (2000) have studied the effects of solid concentration distributions in slurry flow in relation to various flow parameters [37-46]. Many researchers scrutinized the slurry flow process, focusing on the prediction of flow velocity distribution. Some of the contributions in this area involve the work of Wasp al. (1970), Gillies et al. (1991), Doron et al.(1987), Sundqvist et al. (1996), Ghanta and Purohit (1999), Mishra et al.(1998), Wilson et al. (2002) [40,47-52]. Various studies formulated predictions of the pressure drop in a slurry flow process. Similarly, in this area, these were the noteworthy contributors: Masayuki Toda et. al (1972), experimentally investigated the pressure drop in a pipe bend for the solid-fluid slurry flow [53]. Later, Turian and Yuan (1977) formed a pressure drop correlation for the flow of slurries in pipelines in consideration with a stationary bed, heterogeneous flow, saltation flow, and homogeneous flow regime [54]. Moreover, P. Doron et. al (1987) also developed a two layer model for the prediction of pressure drop of a slurry flow of coarse particles

and that too, through horizontal pipelines [48]. Later, Geldart and Ling (1990), Doron and Barnea (1995), Gillis et. al (1991), A. Mukhtar et. al (1995), J. Bellus et. al (2002) Turian et. al (1998), devised different models of the slurry flow through pipes [40, 55-59]. They predicted the pressure drop in relation to various flow parameters that included, concentration distribution, granular pressure effects, velocity distributions, energy effects and turbulence kinetics.

Table 1 presents an overview of the work that has been carried in the field of annular slurry flow (sand and water) in a horizontal pipeline either using Ansys-fluent software or performing practical lab-scale experiments or both. Where, CFD simulations helped to minimize assumptions by using the physics-based Navier–Stokes equations to model the hydrodynamics of the flow system. Also, table-1 shows the different parameters used in each study such as the multiphase and viscous model, the diameter of the horizontal pipe (D), the slurry velocity (v), the solid particle diameter (d_s), the solid particle density (ρ), and the volumetric concentration (C_v%) of the slurry flow.

Table 1. An overview of previous academic research on slurry flow

Reference	Multiphase model	Viscous model	D (mm)	d_s (mm)	$\boldsymbol{\rho}$ (Kg/m^3)	$\boldsymbol{v}$ (m/s)	C_v %
(Gillies & Shook, 1994) [42]			53.2	0.18	2650	3.1	14, 29, 45
(Matousek, 2001) [60]			150	0.12, 0.37, 1.85		2-10	12 - 43
(Kaushal & Tomita, 2002) [61]			105	0.38, 0.91, 1.28, 1.80, 2.55, 7.39		2	4.0, 8.2, 13.5, 18.6
						2.75	12.2, 19.1, 25.8
						3.5	12.2, 18.6, 26.0
(Ling, Skudarnov, Lin, & Ebadian, 2003) [62]	Algebraic slip mixture (ASM)	RNG k–ε turbulent	22.1	0.11	2381 & 4223	1-3	10, 20
(Hernández, Blanco, & Rojas-Solórzano, 2008) [63]	Eulerian multiphase	RNG k–ε turbulent	22.1	0.30	2390	3	5
(Kaushal, Thinglas, Tomita, Kuchii, & Tsukamoto, 2012) [64]	Eulerian multiphase	Standard k– ε	54.9	0.125		1-5	0-5

Reference	Multiphase model	Viscous model	D (mm)	d_s (mm)	ρ (Kg/m^3)	v (m/s)	C_v %
(Vlask, Kysela, & Chara, 2012) [65]			36	6	2540, 2560	1.0-5.5	2.7, 2.9, 6.1, 6.5, 9.7, 10.4
(Nabil, El-Sawaf, & El-Nahhas, 2013) [66]	Eulerian multiphase	Standard k– ε	26.8	0.2, 0.7, 1.4	2650	0.5- 5.0	10-30
(Gopaliya & D.R., 2016) [67]	Eulerian multiphase	RNG k-ε turbulence	263	0.165	2650	3.5	9.95, 18.4, 26.8, 33.8
				0.29	2650	4.0, 4.7	16, 25, 34
				0.55	2650	3.9, 4.4	15, 25, 30
(Ofei & Ismail, 2016) [68]	Eulerian multiphase	Standard k– ε	103	0.09-0.27	2650	5.4	10-40
(Sultan, Rahmana, Zendehboudia, Talimi, & Kelessidis, 2018) (Skudarnov, Lin, & Ebadian, 2004) [69, 70]	Eulerian multiphase	Reynolds Stress Model (RSM)	23	0.14	(2490 & 4200)	1.3-2.3	15
(Sultan, Rahmana, Zendehboudia, Talimi, & Kelessidis, 2018) [69]	Eulerian multiphase	Reynolds Stress Model (RSM)	26	0.165	2650	3.5	9.95, 18.4, 26.8, 33.8
				0.29	2650	4.0,4.7	16, 25, 34
				0.55	2650	3.9	15, 25, 30

Reference	Multiphase model	Viscous model	D (mm)	d_s (mm)	ρ (Kg/m^3)	v (m/s)	C_v %
(Ahmed & Mohanty, 2018) [20]	Eulerian multiphase	RNG k-ε turbulence	54.9	0.125	2470	2, 5	30, 40

2.5 Conclusion of literature review

Overall, investigations of two-phase slurry flow through pipelines aim to develop general solutions based on available experimental data for solid volumetric or mass concentration profiles, pressure gradients and slurry velocity profiles. Various studies scrutinized the flow of Newtonian fluids in annuli to develop empirical and analytical models. However, the novelty of this research work is demonstrated on the presentation of the hydrofracturing fluid pressure issuing off the perforating gun holes, as the fluid pressure is expected to be lower at the outlet holes according to Bernoulli theory. It is evident through the literature review that none of the previous studies investigated or analyzed the slurry flow at the outlet perforated holes, yet many thorough studies have investigated the different parameters of the slurry system in horizontal pipes.

Also, it is noticeable that none of the previous studies have used Particle Image velocimetry (PIV) in which it has a high ability to measure the instantaneous velocity of the particles and diagnose the slurry flow by using non-instructive leaser. Hence, the PIV technology will be utilized in the experimental work of this thesis for a better understanding of the whole slurry flow process.

Furthermore, it is observed that most of the fracturing fluid is using sand particles due to its availability and low unit cost as explained in chapter 1. Consequently, the sand particle will be used as the proppant agent in the research.

Generally, most of the numerical studies in table-1 used Eulerian and RNG k-ε turbulent for the multiphase and viscous model, respectively in which it indicates the effectiveness of these two models in solving the slurry flow system and its parameters such as pressure drop, solid concentration profiles, and deposition velocity.

Finally, it is observed that the studied slurry velocities range from 1 to 10 m/s,

the particle volumetric concentration ranges from 2.7% to 40%, the particle diameter ranges from 0.09 mm to 7.39 mm, and the diameter of the horizontal pipe ranges between 23 mm to 263 mm. These limitations will be taken into consideration in the designing of the slurry flow system in chapter 3.

CHAPTER 3: MATERIAL AND METHODS

This chapter is divided into two main sections; the experimental setup and the numerical simulation. Each part presents the material and methods which have been used to analyze the slurry flow in a horizontal perforated pipeline. Figure 8 presents the flowchart of the thesis approach. Where, selecting a suitable turbulence model between (k-ε, RNG, RSM) is carried through comparing the results against published experimental data. The selected turbulence closure in modeling the slurry flow in a perforated pipe is validated through conducting an experiment in a lab-scale. Throughout the experiment, various issues have occurred (which will be mentioned later), yet some results have been achieved.

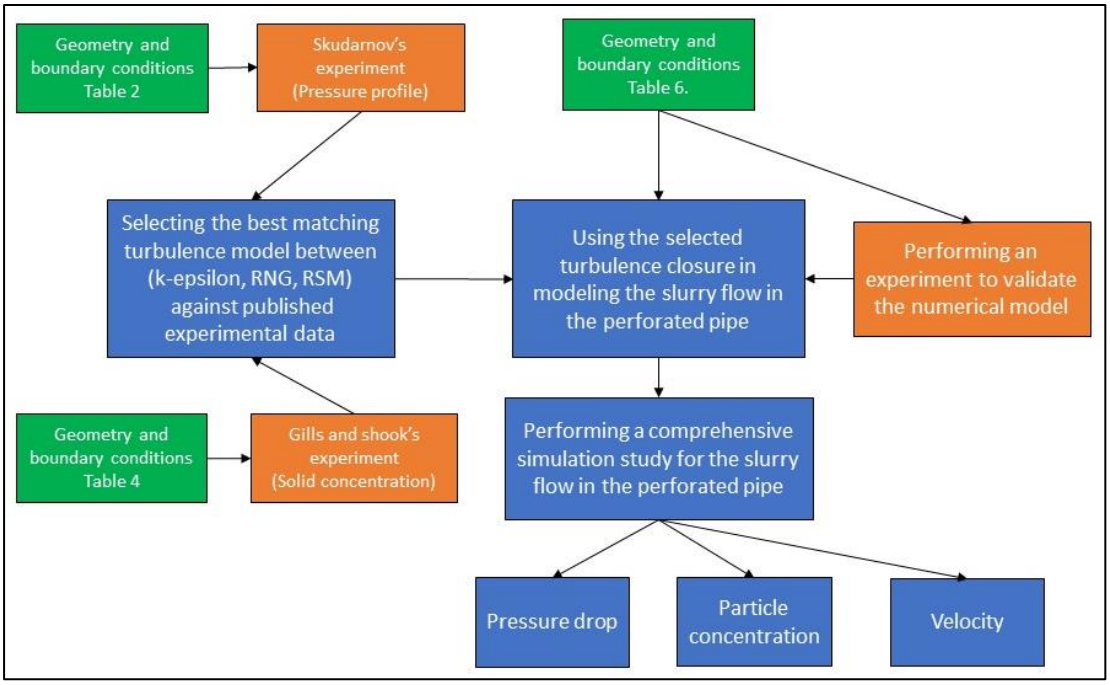

Figure 8. Flowchart of the thesis approach.

3.1 Experiential setup:

A closed loop pipe system, with a test section of clear acrylic pipe, is used to experimentally investigate the slurry flow parameters. The experiment utilized a slurry composed of one size particle dry sand of density of 1442 Kg/m^3 mechanically mixed with water. From an open tank, the slurry was pumped throughout the circuit using a centrifugal pump, Xylem DL-125. A variable frequency speed drive was used to control slurry flow rate. A digital pressure gauge, ASHCROFT 2030 sanitary gauge model, was used to measure the system slurry pressure. The detailed specifications of the pump and the pressure gauge are presented in appendix C and D, respectively.

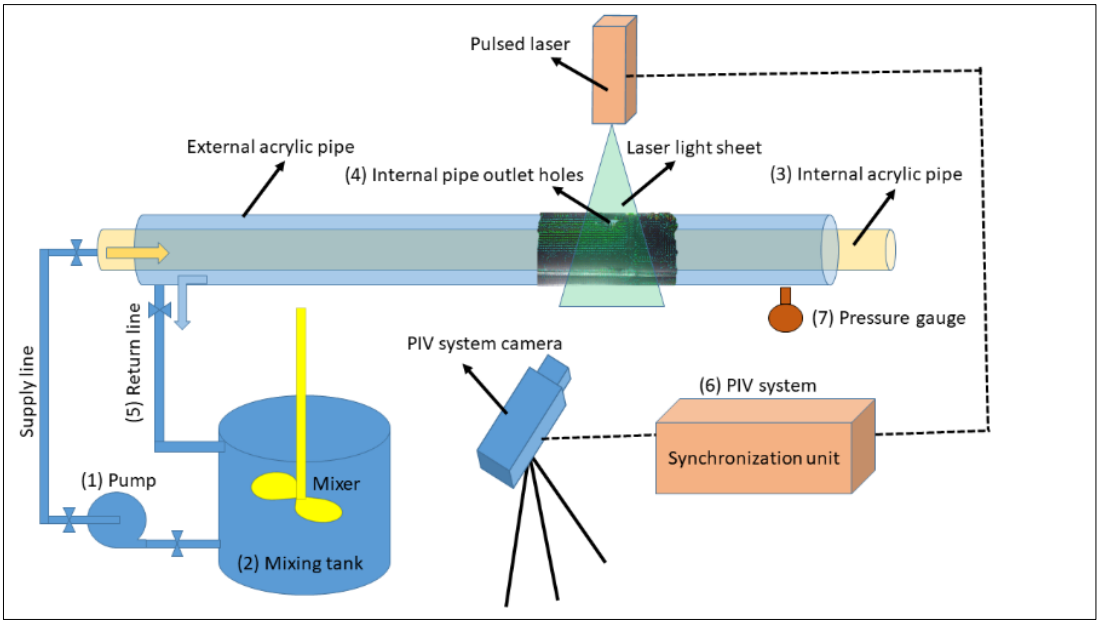

Figure 9. Schematic setup of slurry flow system.

Figures 9 and 10 present the components of the experimental setup used in this study. Component (1) is the DL 125 xylem centrifugal pump with a maximum flow rate of 67.2 GPM and maximum pressure of 152 kPa (Figure 11). Component (2) is

the mixing tank of a capacity of 14.3 gallons, where the sand and water are continuously mechanically mixed. Component (3) is the internal acrylic pipe of dimensions of 2 inches in diameter, 3mm thickness, and 2m long. Component (4) is the outlet gun holes of the internal pipe; four holes are drilled symmetrically with a diameter of 5 mm. Component (5) is the return line of the external pipe with a diameter of 12 mm, where the slurry flow is returned to the mixing tank (2). Component (6) is the Particle image velocimetry (PIV) system which is connected to a computer to non-intrusively record and measure the velocity and visualize the movement of sand particles through the internal perforated gun holes (4). Component (7) is a digital slurry pressure gauge connected to the external pipe near the perforated holes to measure the pressure with an accuracy of 0.25% (Figure 12). Component (8) is the variable frequency drive (VFD); used for adjusting the flow rate and the pressure of the centrifugal pump (1) as required.

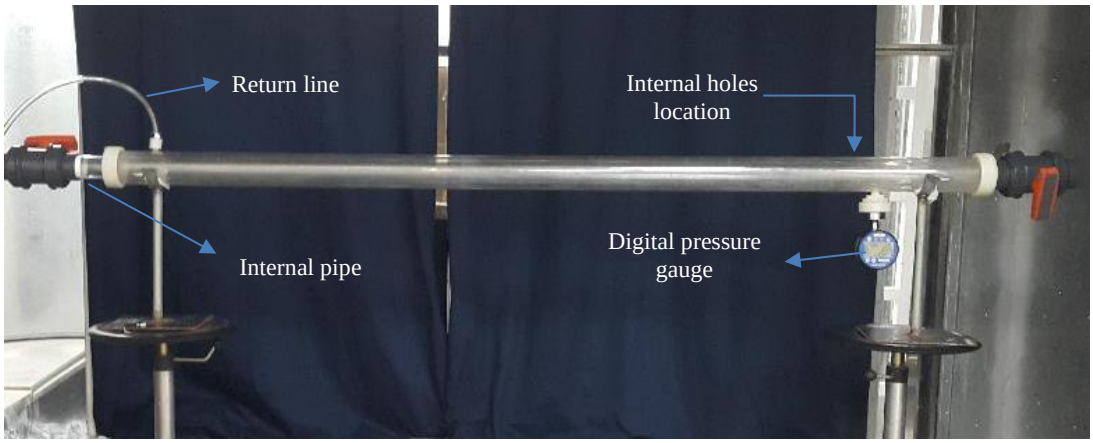

Figure 10. The apparatus of the slurry flow experiment.

Figure 11. DL 125 xylem submersible pump.

Figure 12. Digital slurry pressure gauge.

3.1.1 Velocity measurement using particle image velocimetry (PIV)

Particle image velocimetry (PIV) is an experimental tool to non intrusively obtain the velocity of a whole flow field. PIV is based on detecting the light scattered from the sand as tracer particles contained in the slurry flow. It captures two consecutive images of the sand seeded flow field. Cross correlation of the two images is used to estimate the displacement of each group of sand particles, and from the knowledge of the time between the frames, a corresponding velocity is obtained. The

sand particles are illuminated at two different time instants by means of a double pulsed laser sheet. The laser used is Dantec Dynamics DualPower 200-15, which is a twin cavity Nd:YAG laser. Wavelength is 532 nm, and the pulse duration is 4 ns. Maximum laser power is 1200 mJ. For processing the acquired images and the results, DynamicStudio software is used. The camera used is a CCD camera, which is the FlowSense EO 4M from Dantec Dynamics, with a resolution of 2048×2048 pixels. In order to obtain the velocity field, a set of 50 double frame images were acquired at a triggering frequency of 7.4 Hz, which spans a period of 6.75 seconds. The time between the light pulses, which is also the time between the two frames of a double frame image, was $1000\ \mu sec$. Each double frame image resulted in a velocity field. Hence, 50 velocity fields were obtained and averaged to obtain the final flow filed velocity. The interrogation window size was 32×32 pixels with a 50% overlap in both the horizontal and vertical directions, which resulted in a map of 127×127 vectors map (Figure 13) [71].

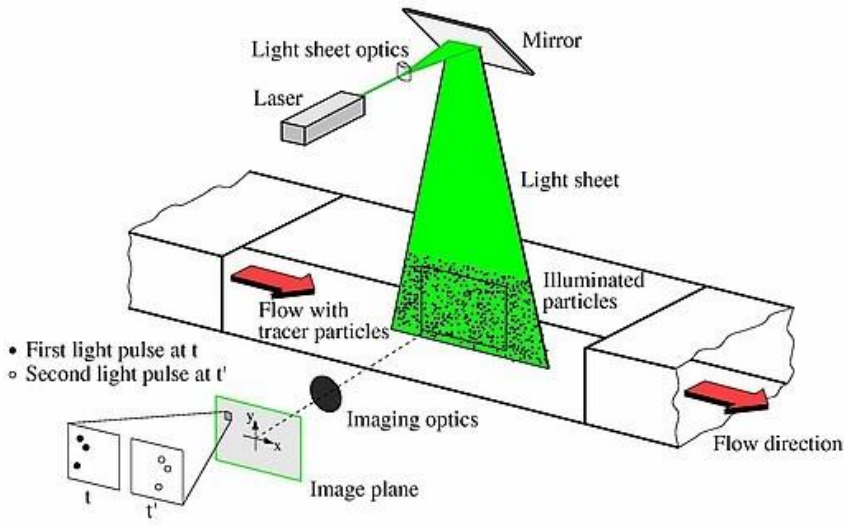

Figure 13. Typical 2-D PIV setup [71].

3.1.2 The slurry system design of the experiment

The design of the slurry system experimental set up was based on several factors such as the internal pipe diameter and the particles size of the dry sand. In his experimental study of a slurry system, Gopaliya (2016) reported that the pressure gradient of slurry flow in a horizontal pipeline, of an internal diameter D, becomes almost constant after a length of 25-30D downstream [67]. To ensure a fully developed flow, the gun holes of the internal pipe were drilled at about 33D of the internal pipe length. The internal perforation holes were drilled about 1.7m downstream of the pipe inlet. The diameter of the internal pipe perforation holes was drilled based on the range of the most commercial perforating gun punch holes which were in (0.23 in to 0.72 in) range [72]. The lowest reported mean value of sand particle diameter in well stimulation was about 500 microns [4]. Using an auto sieve shaker (Figure 14), in this experiment, the dry sand particles were sieved to limit the range of sand particle size between 425 microns and 600 microns [73].

Figure 14. Auto sieve shaker.

3.1.3 The challenges of slurry experiment:

Finding a suitable pump for the slurry system was the most challenging part of the experimental work due to their unavailability in Qatar Market and their high cost in the international market. Moreover, the selected pump from Italy failed two times due to a malfunction in the seal system as a result, few results have been achieved, and they were not sufficient to build facts or to establish a full conclusion. Also, the process of manufacturing the pipe, and assembling the parts from different places were a big challenge to make the slurry system. Finally, the laboratory space was not enough to make a larger model with a larger pump, so the space element was also a factor in the system designing. Therefore, the focus was on simulation in order to compensate for the major shortfall in practical experience. However, some results were extracted from the experiment which supports the simulation process and proves its validity.

3.2 Numerical simulation

Computational Fluid Dynamics (CFD) techniques were used to study slurry flow in a horizontal pipeline. CFD is based on solving the relevant equations of motion by numerical methods. Recent improvements in numerical procedures, in meshing schemes and in computational power made it possible to consider large and complicated simulations.

ANSYS- Fluent is used as a simulation tool in many industrial applications due to its physical modeling capabilities to model flows, turbulence, reactions and heat transfer. FLUENT software was tested using experimental data of various research and proved its ability to perform detailed simulations and generate matching results when using appropriate methods and high-quality mesh [74]. This study used the commercially available CFD software ANSYS-Fluent to perform the numerical

simulations of the slurry flow in a horizontal pipe. Assigning appropriated boundary conditions, all governing equations of slurry flow were solved in a Cartesian coordinate system.

3.2.1. Mathematical models

Selection of an appropriate viscous model is foremost important in the CFD analysis of slurry flows. The selection depends mainly on the flow Reynold number and the range of volume fraction (α) of the flow solid phase. Since Reynold number, considered in this study, is higher than 500,000, the type of the flow is considered as turbulent.

In the literature review section, most of the studies used Eulerian model to simulate several types of slurry flow through different pipe diameters. For each phase, the Eulerian model solves the momentum equations in a segregated method. Ansys Fluent algorithm solves the total pressure of multiphase for a wide range of flows due to the shared pressure of the multiphase flow and volume fraction equations. Additionally, solving the implemented phase coupled (SIMPLE) in an implicit manner rather than explicit, offers a robust solution to the multiphase system.

In this research, granular version of the Eulerian model with implicit calculations was adopted for calculating the different parameters of the slurry flow. The Granular version is capable of capturing the effect of friction and collisions between the sand particles which is an important phenomenon in higher concentration slurry flows of different particle sizes. Granular viscosity and frictional viscosity were modeled using Syamlal-Orbien and Schaeffe model respectively [75]. Drag and lift coefficients in the phase interaction were calculated based on the equations of Schiller-Naumann and Moroga [75].

3.2.1.1 Mixture theory approach

The description of Eulerian multiphase flow is account for dispersed-continuous phase interaction in which it incorporates with the concept of phasic volume fractions, denoted by (α_q). Volume fractions represents dispersed phase dissolved in each continuous phase, and the laws of conservation of mass and momentum are satisfied by each phase individually. The mixture theory approach can be used for the derivation of the conservation equations. The volume of phase q. Where, q is either solid (s) or fluid (f), v_q, is defined by [75]

$$v_q = \int_V \alpha_q dv \qquad \ldots (11)$$

Where

$$\sum_{q=1}^{n} \alpha_q = 1 \qquad \ldots (12)$$

The effective density of slurry flow ($\dot{\rho_q}$) is

$$\dot{\rho_q} = \alpha_q \rho_q \qquad \ldots (13)$$

Where, ρ_q is the physical density of phase. The volume fraction equation is solved through implicit time discretization.

3.2.1.2 The continuity equation

$$\frac{\partial}{\partial t}\left(\alpha_q \rho_q\right) + \nabla.\left(\alpha_q \rho_q \overrightarrow{v_q}\right) = 0 \qquad \ldots (14)$$

Where, $\overrightarrow{v_q}$ is the velocity vector of phase q.

3.2.1.3 The momentum balance for fluid phase*:*

$$\frac{\partial}{\partial t}\left(\alpha_f \rho_f \vec{v}_f\right) + \nabla.\left(\alpha_f \rho_f \vec{v}_f v_f\right)$$
$$= -\alpha_f \nabla P + \nabla.\bar{\bar{\tau}}_f + \alpha_f \rho_f \vec{g} + K_{sf}\left(\vec{v}_s - \vec{v}_f\right) + \vec{F}_{lift,f}$$
$$+ C_{vm}\alpha_f \rho_f (\vec{v}_s.\nabla\vec{v}_s - \vec{v}_f \nabla\vec{v}_f) \quad \ldots (15)$$

3.2.1.4 The momentum balance for solid phase:

$$\frac{\partial}{\partial t}(\alpha_s \rho_s \vec{v}_s) + \nabla.(\alpha_s \rho_s \vec{v}_s \vec{v}_s)$$
$$= -\alpha_s \nabla P_s + \nabla.\bar{\bar{\tau}}_s + \alpha_s \rho_s \vec{g} + K_{fs}\left(\vec{v}_f - \vec{v}_s\right) + \vec{F}_{lift,s}$$
$$+ C_{vm}\alpha_s \rho_f (\vec{v}_f.\nabla\vec{v}_f - \vec{v}_s \nabla\vec{v}_s)$$
$$\ldots (16)$$

Where;

∇P: is the static pressure gradient.

∇P_s: is the solid pressure gradient or the inertial force due to particle interactions.

$\nabla.\bar{\bar{\tau}}$: is viscous forces, where $\bar{\bar{\tau}}_f$ and $\bar{\bar{\tau}}_s$ are the stress-strain tensors for fluid and solid, respectively.

$\rho_s \vec{g}\ and\ \rho_l \vec{g}$: are body forces, where ρ is the density and $\vec{g}$ is acceleration due to gravity.

$K_{fs}\ and\ K_{sf}$: are inter-phase drag force coefficient caused by the velocity difference between the velocity of fluid $\vec{v}_f$ and solid $\vec{v}_s$ phases.

$\vec{F}_{lift}$: is the lift force.

$C_{vm}\alpha_s \rho_f (\vec{v}_f.\nabla\vec{v}_f - \vec{v}_s \nabla\vec{v}_s)$: is the virtual mass force. Since in most of the multiphase applications, the effective particle radius is very small as compared to the velocity

scale, virtual mass effects can be observed predominantly only at relatively high efflux concentrations. It is therefore, a value of 0.5 (default value) is adopted for C_{vm} in the present study [75]:

$\bar{\bar{\tau}}$ is expressed as follow [75]:

$$\bar{\bar{\tau}} = \alpha_q \mu_q \left(\nabla \vec{V}_q + \nabla \vec{V}_q^T\right) + \alpha_q \left(\lambda_q - \frac{2}{3}\mu_q\right) \nabla . \vec{V}_q \bar{\bar{I}} \qquad \ldots (17)$$

Where;

$\bar{\bar{I}}$ indicates identity tensor λ_q represents bulk viscosity of the solid

μ_q and λ_q are the shear and bulk viscosity of phase q,

3.2.1.5 Turbulent Models

Turbulence models are classified according to the applied governing equations (Reynolds-averaged Navier-Stokes or Large Eddy Simulation equations). Within these broader categories, turbulence models are further broken down by the number of additional transport equations which must be solved in order to compute the model contributions. The most common turbulence model is the k-ε model. However, there are many other models in this caption. The k-ε model is called a family of models. Specialized versions were developed for various specific flow configurations. Some of the more common variants include the RNG k-ε models [76].

3.2.1.5.1 Standard k-ε Model

The standard k-epsilon (k-ε) turbulence model is used to simulated mean flow characteristics for turbulent flow conditions. The turbulence models implemented in this thesis belong to the class of two equations k-epsilon models. The original impetus for the k-ε model was to improve the mixing-length model, as well as to find an alternative to algebraically prescribing turbulent length scales in moderate to high

complexity flows. The model assumes that the ratio between Reynolds stress and mean rate of deformations is the same in all directions. The turbulence closure is achieved using two transport PDEs for the turbulence kinetic energy k and turbulence dissipation ε scalars [75, 76]:

For turbulent kinetic energy k:

$$\frac{\partial(\rho K)}{\partial t} + \frac{\partial(\rho k u_i)}{\partial x_i} = \frac{\partial}{\partial x_j}\left[(\mu + \frac{\mu_t}{\sigma_k})\frac{\partial K}{\partial x_j}\right] + G_k + G_b - \rho\varepsilon \quad \ldots (18)$$

For dissipation ε:

$$\frac{\partial(\rho\varepsilon)}{\partial t} + \frac{\partial(\rho\varepsilon u_i)}{\partial x_i} = \frac{\partial}{\partial x_j}\left[(\mu + \frac{\mu_t}{\sigma_\varepsilon})\frac{\partial \varepsilon}{\partial x_j}\right] + C_{1\varepsilon}\frac{\varepsilon}{k}(G_k + C_{3\varepsilon}G_b) - C_{2\varepsilon}\rho\frac{\varepsilon^2}{k} \quad \ldots (19)$$

Where,

u_i represents velocity component in corresponding direction

G_k represents the generation of turbulence kinetic energy due to the mean velocity gradients.

G_b is the generation of turbulence kinetic energy due to buoyancy.

σ_k and σ_ε are the turbulent Prandtl numbers for k and ε , respectively.

The turbulent or eddy viscosity μ_t is represented in terms of two turbulence variables, the turbulence kinetic energy k and its rate of dissipation (ε):

$$u_t = \rho C_\mu \frac{k^2}{\varepsilon} \quad \ldots (20)$$

Equations (18, 19, and 20) consist of some adjustable constants (σ_k, σ_ε, $C_{1\varepsilon}$, $C_{2\varepsilon}$, C_μ). The values of these constants have been arrived at by numerous iterations of data fitting for a wide range of turbulent flows. These are as follows:

$$\sigma_k = 1.00,\ \sigma_\varepsilon = 1.30,\ C_\mu = 0.09$$

$$C_{1\varepsilon} = 1.44,\ C_{2\varepsilon} = 1.92$$

3.2.1.5.2 RNG k-ε Model

The RNG-based k-ε turbulence model is derived from the Navier-Stokes instantaneous equations, using a mathematical technique called "renormalization group" (RNG) methods. RNG theory provides an analytically derived differential correlation for turbulent Prandtl numbers that accounts for low Reynolds number effects. while the standard k- ε model uses constant values. The main difference between the RNG model and standard k-ε model lies in the additional term in the ε equation that improves the accuracy for rapidly strained flows, given by [75,76]:

$$R_\varepsilon = \frac{C_\mu \rho \eta^3 (1 - \frac{\eta}{\eta_0})}{1 + \beta \eta^3} \frac{\varepsilon^2}{k} \qquad \ldots (21)$$

Where $\eta = Sk/\varepsilon$, $\eta_0 = 4.38$, $\beta = 0.012$. The constant parameters used indifferent equations are taken as $C_{1\varepsilon} = 1.42$, $C_{2\varepsilon} = 1.68$, $C_{3\varepsilon} = 1.2$, $\sigma_k = 1.0$, $\sigma_\varepsilon = 1.3$

3.2.1.5.3 Reynolds Stress Equation Model

Reynolds stress equation model (RSM), also known as second-order or second-moment closure model is the nearly most complex classical turbulence model. The exact transport equation for the Reynolds Stress Model (RSM) is [75]:

$$\underbrace{\frac{\partial}{\partial t}(\rho\overline{u_i'u_j'})}_{local\ time\ derivative} + \underbrace{\frac{\partial}{\partial x_k}(\rho u_k\overline{u_i'u_j'})}_{C_{ij}=convection}$$

$$= \underbrace{-\frac{\partial}{\partial x_k}[\rho\overline{u_i'u_j'u_k'} + \overline{\rho'(\delta_{kJ}u_i' + \delta_{\iota k}u_j')}]}_{D_{T,ij}=Turblent\ diffusion} + \underbrace{\frac{\partial}{\partial x_k}[\,\mu\frac{\partial}{\partial x_k}(\overline{u_i'u_j'})]}_{D_{L,ij}=Molecular\ diffusion}$$

$$- \underbrace{\rho(\overline{u_i'u_k'}\frac{\partial u_j}{\partial x_k} + \overline{u_j'u_k'}\frac{\partial u_i}{\partial x_k})}_{P_{i,j}=Stress\ Production} - \underbrace{\rho\beta\left(g_i\overline{u_j'\theta} + g_j\overline{u_i'\theta}\right)}_{G_{ij}=\ Buoyancy\ production}$$

$$+ \underbrace{p\left(\frac{\partial u_i'}{\partial x_j} + \frac{\partial u_j'}{\partial x_i}\right)}_{\varphi_{ij}=\ Pressure\ strain} - \underbrace{2\mu\frac{\partial u_i'}{\partial x_k}\frac{\partial u_j'}{\partial x_k}}_{\epsilon_{ij}=\ Dissipation}$$

$$- \underbrace{2\rho\Omega_k\left(\overline{u_j'u_m'}\epsilon_{ikm} + \overline{u_i'u_m'}\epsilon_{jkm}\right)}_{F_{ij}=\ Production\ by\ system\ Rotation} \qquad \ldots (22)$$

The various terms in these exact equations, C_{ij},$D_{L,ij}$, P_{ij},and F_{ij} do not require any modeling. However, $D_{T,ij}$, G_{ij}, φ_{ij}, and ε_{ij} need to be modeled to close the equations.

CHAPTER 4: RESULTS AND DISCUSSION

In this chapter, selecting a suitable turbulence model for this study will be carried through comparing the numerical results of the pressure gradient and the solid concentration profile for a slurry flow in a horizontal pipe against several published experimental studies using three different turbulent models (Standard k-ε, RNG k-ε, and RSM). Hence, the best matching turbulent closure model with the published experimental data is selected for further simulation of the slurry flow of a perforated pipe. In the second part of the research, the result acquired from the laboratory experiment of a slurry flow in a horizontal perforated pipe are utilized to support the validity of the selected turbulence model.

4.1 Selecting a suitable turbulence closure

4.1.1 Pressure gradient verification:

The mean slurry pressure gradient is an important parameter in slurry transportation and pipeline design. Skudarnov et al. (2001) and Newitt et al. (1955) [77, 78] conducted laboratory scale experiments of slurry flow of different sand-water mixtures in horizontal pipe of 1.4 m long and an internal diameter of 0.0221 m [62]. Their experimental data, as reported by Ling et al. (2003), were compared with the numerical results generated from the three Ansys-Fluent turbulence models.

The Eulerian multiphase with standard k-ε turbulence model was used to simulate the slurry flow where the secondary phase (sand particles) was modeled as spherical granular particles. The three models were set up with the following boundary conditions; a volume concentration of solids in the slurry of 20%, a solid density of 2381 kg/m^3, a mean diameter of the sand particles of 0.099 mm, and a slurry flow mean velocity range of 1 to 3 m/s. The geometry and the boundary conditions, as reported by Skudarnov et al. (2001) and Newitt et al. (1955), are shown

in Table 2.

Table 2. Skudarnov et al. and Newitt geometry and boundary conditions [62]

Parameter	value	Parameter	Value
Pipe length	1.4 m	Silica sand density	2381 Kg/m^3
Pipe diameter	0.0221 m	Mean particle diameter	0.099 mm
Slurry type	Water + Silica sand	Solid volumetric concentration	20%
Water density	998.2 kg/m^3	Mean slurry velocity	1–3 m/s

The structured mesh of Skudarnov et al. (2001) and Newitt et al. (1955) model was generated using Ansys-Fluent mesher. In 2003, Ling et al. assessed the Skudarnov and Newitt slurry model and found that the level of tolerance of the grid system was acceptable when using about 184,000 cells [62]. Therefore, this study considered a 1.2 million cells model to ensure a satisfactory solution for the slurry flow. The maximum face size of the grid did not exceed 0.001 m and the minimum face size was set to 0.00021 m. The average quality of the model mesh was 81% (Figure 15).

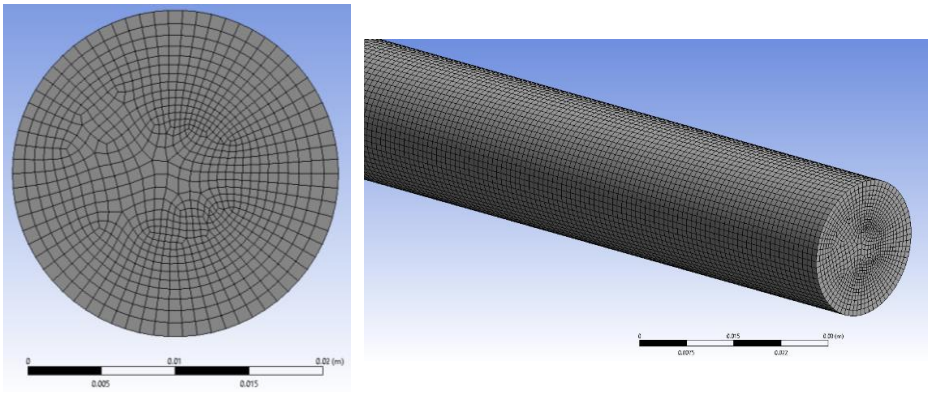

Figure 15. 2D and 3D meshed geometry of Skudarnov and Newitt experiment.

As shown in figure 16, the slurry mean velocity obtained from the experimental data and the numerical results of the three models was higher than the critical deposition velocity. Table 3 summarizes the percentage difference of the mean slurry pressure gradient obtained by the three numerical models at 20% volumetric concentration. Among the three numerical models, the difference between the numerical results of the standard k-ε and the experimental data was the highest in comparison to the numerical results of the RNG and RSM models. It is evident that the RSM and RNG model results yielded the lowest average root mean square (RSM) percentage difference in comparison to Skudarnov's experimental data. An error of about 5%, specifically at the lower slurry mean velocity, could be critical when calculating the pressure drop in different applications [79, 80]. Hence, the standard k-ε numerical model was eliminated. The RSM and the RNG k- ε numerical models concentration analysis of different slurry volumetric concentrations were assessed.

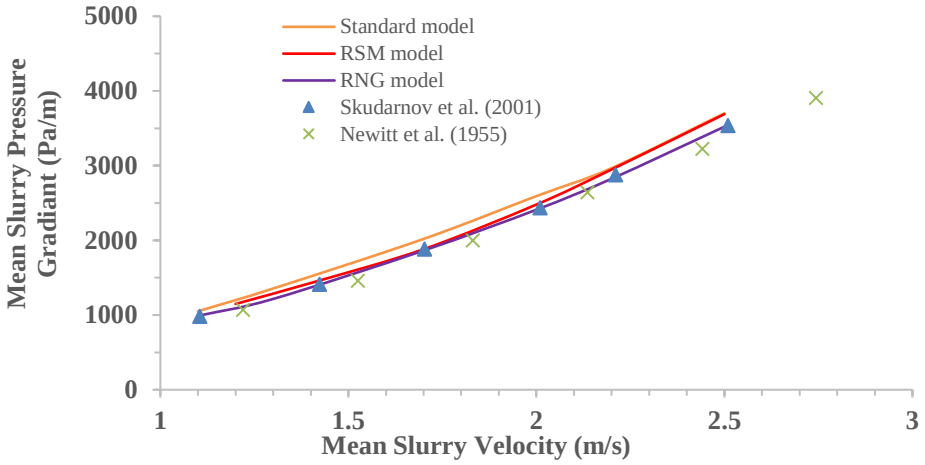

Figure 16. Comparisons of the numerical solution with the experimental data from Skudarnov et al. (2001) and Newitt et al. (1955) in fully developed turbulent flow (ρ= 998.2 kg/m^3, d= 0.0221 m, dp= 0.099 mm). Silica sand–water slurry, ρ = 2381 kg/m^3, concentration= 20% [62].

Table 3. Statistical comparison of mean slurry pressure gradient between Standard k-ε, RSM, and RNG in accordance with Skudarnov et al. (2001)

Volumetric concentration	Root mean square (%)		
	Standard	RSM	RNG
20%	6.55	2.72	0.70

4.1.2 Solid concentration verification:

The local solid concentration profile of a water-sand slurry in a horizontal pipe is calculated using the numerical Reynolds stress model (RSM) and RNG k- ε model. The Eulerian model was used for calculating the parameters of the multiphase flow. For selecting a best matching model, results of the RSM and the RNG k- ε model were compared with the experimental data published by Gillis and Shook (1994) [42,

69]. Table 4 summarizes the geometry and the boundary conditions of Gillis and Shook experiment

Table 4. Gillis and Shook geometry and boundary conditions [69]

Parameter	value	Parameter	Value
Pipe length	2.7 m	Silica density	2650 Kg/m^3
Pipe diameter	53.2 mm	Mean particle diameter	0.18 mm
Slurry type	Water + Silica	wall material	Aluminum
Water density	982 Kg/m^3	Wall roughness	0.2mm
Water viscosity	0.001003 Kg/m.s	Solid volumetric concentration	14%, 29%, 45%
Slurry velocity	3.1 m/s		

The structured mesh system of Gillis and Shook (1994) model is generated using the Ansys-Fluent mesher. Refinement mesh with 100 edge sizing was used to enhance the meshing quality near the walls in addition to fixing the generated maximum face sizing to 0.005 m. The average quality of the mesh was 83% and the number of elements was about 2.6 million (Figure 17).

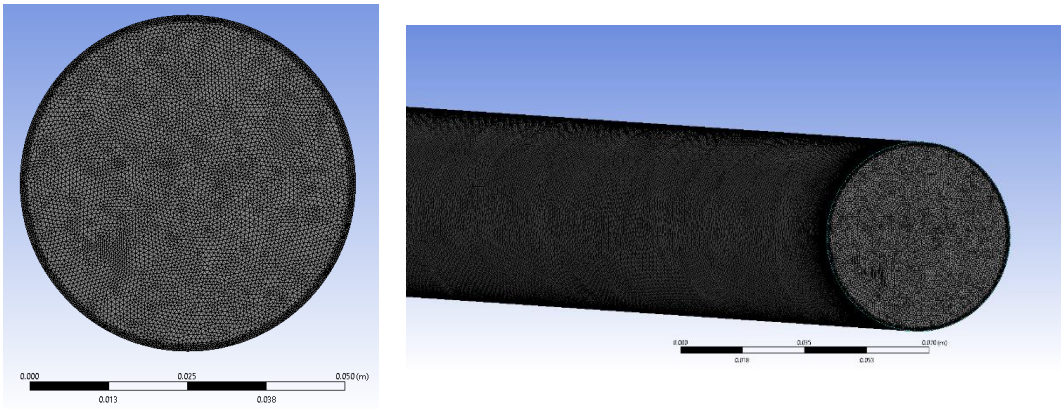

Figure 17. 2D and 3D meshed geometry of Gillis and Shook experiment

Using three different slurry volumetric concentrations of 14%, 29%, 45%, figure 18 and figure 19 show a comparison of concentration profiles obtained from Gillis and Shook (1994) experimental data and the simulation results of the RSM and RNG turbulence models. Generally, the simulated radial concentration values deviated from experimental data as sand concentration increased. In particular, near the walls in the lower half of the pipe cross-section. This deviation is attributed to the abrasive rounding of the large size sand particles from repeated system circulation during the experiment. This is resulting in significant generation of finer sand particles distributed uniformly within the pipe. This would have led to a possible increase in carrier density. The simulations were carried at a mixture velocity of 3.1 m/s.

Table 5 depicts the root mean square (RMS) of the percentage difference between Gillis and Shook experimental data and the simulation results. It is clear that the results obtained off the RNG k- ε model agreed better than their RSM model counterparts for the three different slurry volumetric concentrations of 14%, 29%, 45%. This result infers that the RNG K- ε model is more suited model for the slurry

flow analysis. Therefore, in this paper, the RNG k- ε numerical model is selected to simulate the slurry flow.

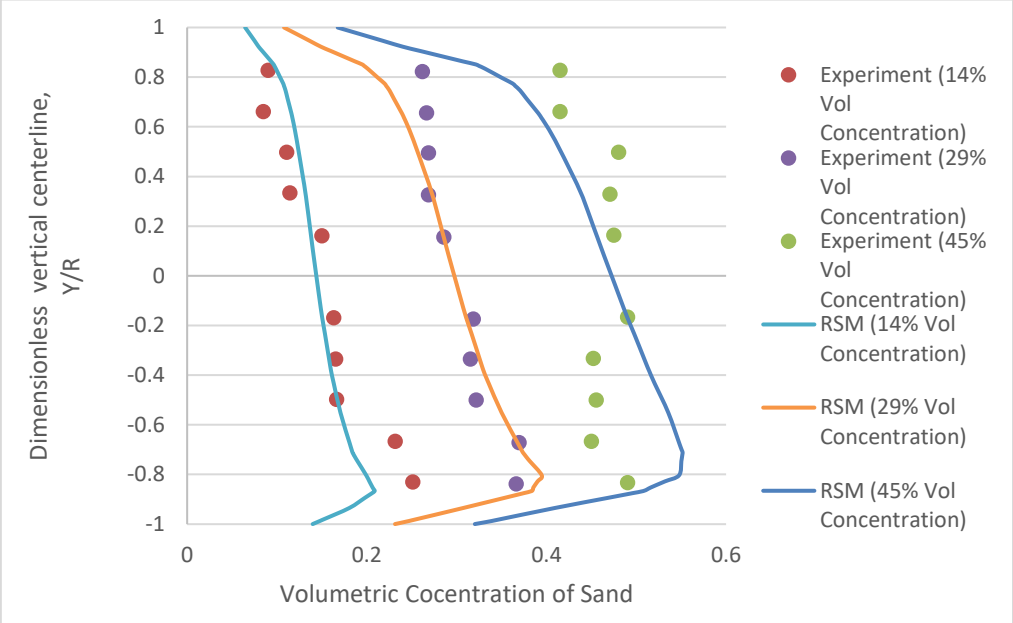

Figure 18. Comparison between RSM model and experimental data of concentration profile for different slurry volumetric concentration at mixture velocity of 3.1 m/s [69].

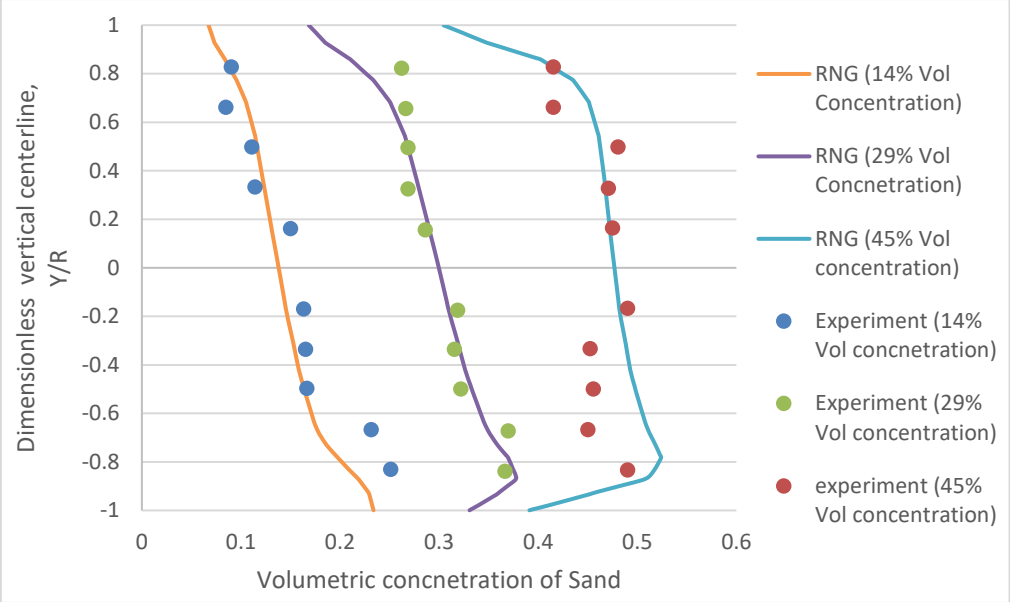

Figure 19. Comparison between RNG model and experimental data of concentration profile for different slurry volumetric concentration at mixture velocity of 3.1 m/s [69].

Table 5. Statistical comparison of concentration profile between RSM and RNG

Volumetric concentration	Root mean square (%)	
	RSM	RNG
14%	9.76	7.95
29%	6.17	4.20
45%	6.60	4.37

4.2 The framework of the numerical model for the slurry flow in a horizontal perforated pipe

4.2.1 Grid independent test:

A CFD meshed model must be assessed using an appropriate grid

independence method. Otherwise, the numerical results must be vigorously compared to their experimental counterpart to ensure an acceptable level of accuracy. Grid independence is performed by varying the model mesh size from coarser to finer while monitoring the output results of each meshed model. When the acquired numerical results are not affected by increasing the model mesh size, then the model is selected to perform the final solution. Figure 20 shows that the pressure drop variation of two-phase (sand and water) flow in horizontal pipe of 2 m long and 50.8 mm internal diameter are not significant after using 0.008m face element size and 66780 meshed elements. Hence, the mesh face sizing of the inner tube should be less than 0.008m.

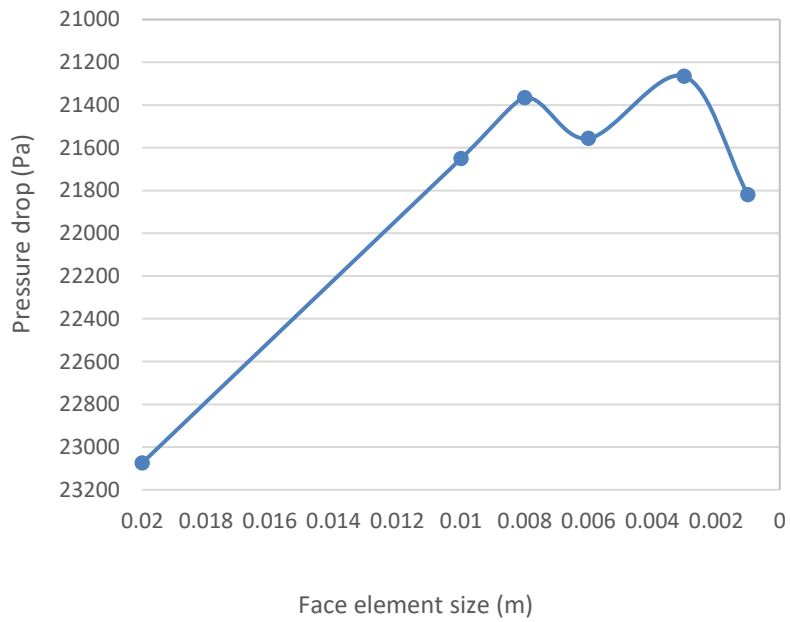

Figure 20. Grid independent test of the slurry flow in horizontal pipe with 2 m long and 50.8 mm internal diameter.

4.2.2 Geometry model and meshing

The three-dimensional (3D) horizontal pipe geometry was modeled using ANSYS 18.0 Workbench Design Modeler. The dimensions of the geometry were designed according to the slurry system of the experimental work as explained in method section. Where, the horizontal internal pipeline was of 2 m long, 50.8 mm internal diameter. Four symmetrical perforated holes of 5 mm diameter were punched about 1.7 m of its length) (Figure 21).

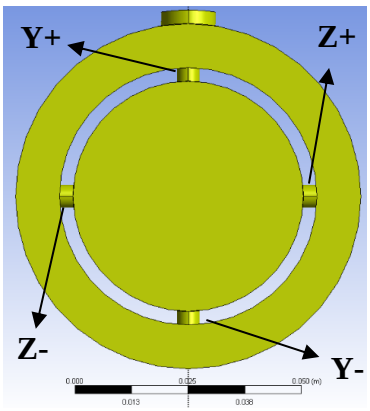

Figure 21. 2D geometry of the thesis experimental work

The grid-independent test yielded a face element less than 0.008 m with 66780 elements. To increase the quality of the model mesh, the mesh count was increased to 2.43 million elements with a maximum face size of 0.002m. Additionally, 90 divisions of edge sizing were applied to the internal pipe. Furthermore, meshing of the four perforated holes was enhanced by using a face size of 0.0003 m (figure 22).

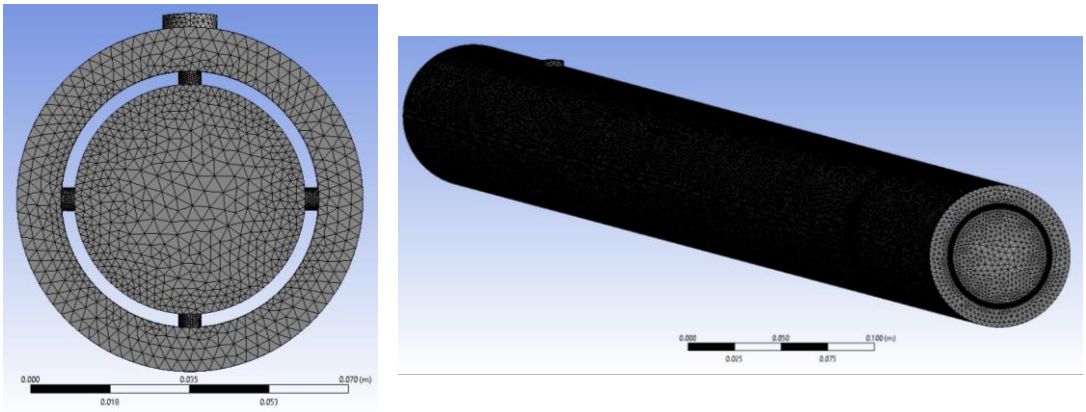

Figure 22. 2D and 3D meshed geometry of the thesis experimental work

4.2.3 Numerical equations selection for this thesis.

The Eulerian model, which considers the continuous liquid phase and the dispersed solid phase as an interpenetrating continuum, is used to model the slurry flow. The Eulerian model is suited for high volume fractions of the dispersed phase which is averaged over each control volume.

The RNG k-ε model is an enhanced model of the standard k- ε model. The model proved its efficacy and accuracy as it has been extensively used for simulation of various processes. This study characterized the RNG k-ε model to be the best suited model for slurry flow simulations. Hence, in this study, the turbulence flow calculations were modeled using the RNG k-ε model with a scalable wall function. Granular viscosity and frictional viscosity were modeled using Syamlal-Orbien and Schaeffe, respectively. Drag and lift coefficients in the phase interaction were calculated based on the equations of Schiller-Naumann and Moroga [73].

4.2.4 Model validation:

For further assessing the RNG k-ε numerical model, a three-dimensional CFD numerical model was developed mimicking a laboratory scale experimental setup.

Hence, the numerical model results were compared to the experimental results. As presented in Table 6, an acrylic pipe of 2 m long, internal pipe diameter of 50.8 mm and wall roughness of 0.002mm was punched with four perforated gun holes each of 5mm in diameter. Dry sand of mean particle diameter of 500 μm and density of ρ_s = 1442 kg/m3 was mixed with water with a particle volume fraction of Cv = 0.05. The inlet mixture pressure was set to 150 kPa and the outlet mixture pressure for the outlet zone is defined as atmospheric pressure.

Table 6. Geometry and boundary conditions of the numerical and the experimental work of the thesis.

Parameter	Value	Parameter	Value
Pipe length	2.0 m	Mean particle diameter	500 μm
Pipe diameter	50.8 mm	Wall material	Acrylic pipe
Diameter of perforated holes	5.0 mm	Wall roughness [81]	0.002 mm
Slurry type	Water + sand	Solid volumetric concentration	5%
Water density	998.2 Kg/m^3	Inlet mixture pressure gauge	150 kPa
Water viscosity	0.001003 Kg/m.s	Outlet mixture pressure gauge	Atmospheric pressure
Sand density	1442 Kg/m^3		

The result of the RNG k-ε numerical model shows that the sand particles precipitated in close proximity to the inlet boundary after 1.5 seconds (Figure 23). This behavior of sand precipitation agreed with the result obtained from the PIV experiment, as the sand was deposited near the inlet of the pipe. The PIV results did not detect any quantities of sand issuing out of the perforated holes (figure 24). Figure 24 and figure 25 show the velocity vectors of the experimental and the numerical results of the slurry flow at 150 kPa. The experimental and numerical results exhibited a fairly flat velocity distribution across the inner pipe section. The velocity of the fluid in contact with the inner pipe wall was almost zero and increases further away from the wall towards the pipe center. The velocity value near the perforated holes was significantly higher than other locations complying with Bernoulli's theory. Due to the drastic reduction in the radius of the flow path at the perforated holes, vortices were formed downstream of the perforated holes as depicted in figures 24 and 25. Qualitatively, the fluid pressure was low at the high velocity areas in full agreement of the Bernoulli theory.

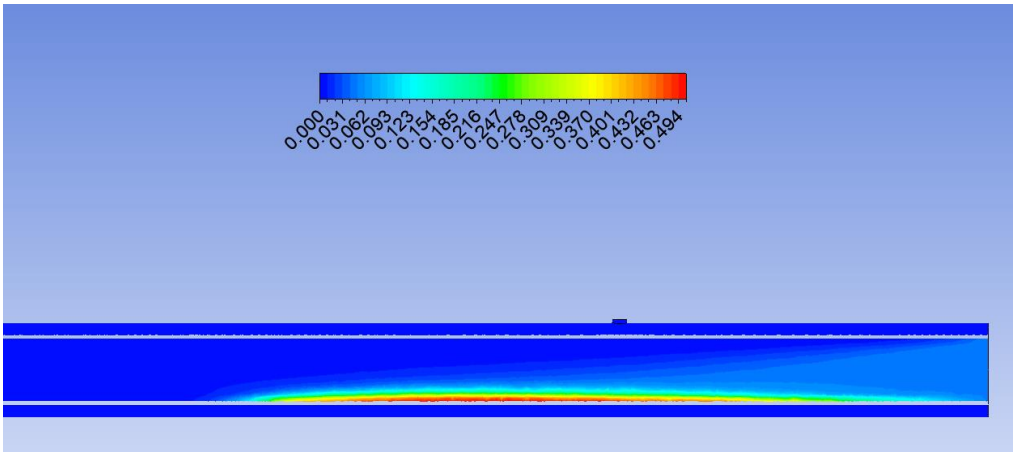

Figure 23. Contour plot of particle concentration in horizontal pipe with inlet boundary.

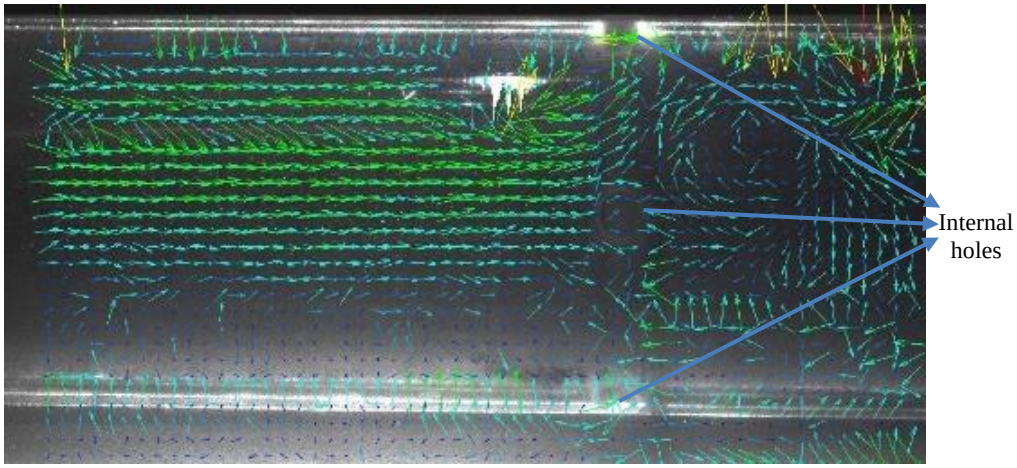

Figure 24. Velocity vector of the slurry system experiment using PIV (At boundary condition of 150 Kpa).

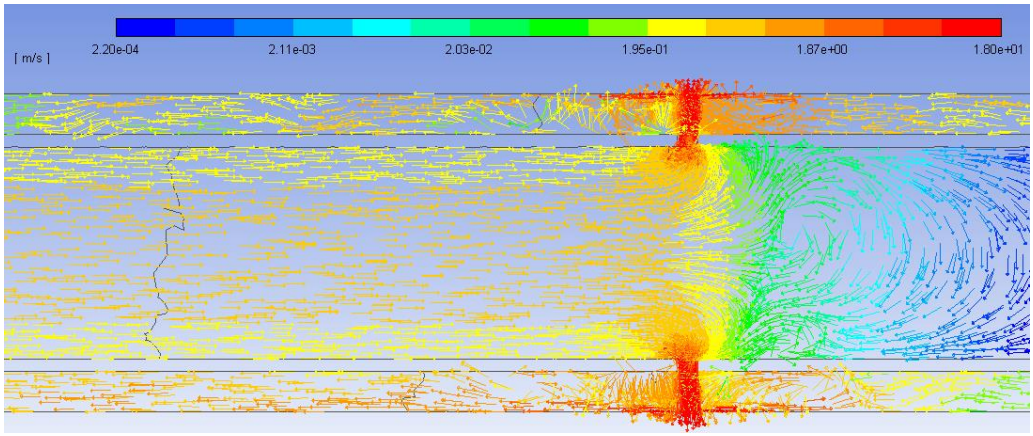

Figure 25. Velocity vector of the simulated slurry system using ANSYS-fluent (at boundary condition of 150 Kpa).

The normalized velocity profile of the slurry flow, obtained experimentally and numerically, is presented in figure 26. The results of the RNG k-ε numerical model and the PIV experimental data exhibited almost asymmetrical distribution with maxima depicted at the center of the pipe annuli. The experimental velocity values were lower than the simulation results at the bottom section of the pipe. This anomaly aroused due to the complex geometry of the double pipe experimental set up and the reflection of the PIV laser sheet of the acrylic lower pipe boundaries. The laser sheet reflection off the annulus, the void between the inner pipe and the outer pipe, impeded the camera ability to capture the fluid velocity of the inner pipe without a reflection glare. As a result, the experimental velocity measurements, conducted using the PIV system, showed some irregularity at the lower section of the double pipe setup. As illustrated in figure 26, the difference between the experimental and numerical normalized velocity values was less than 5% at the upper section of the pipe (zone 1) and almost 10% near the upper inner wall (zone 2). The normalized velocity profile was further used for validation of the RNG k-ε numerical model simulation results.

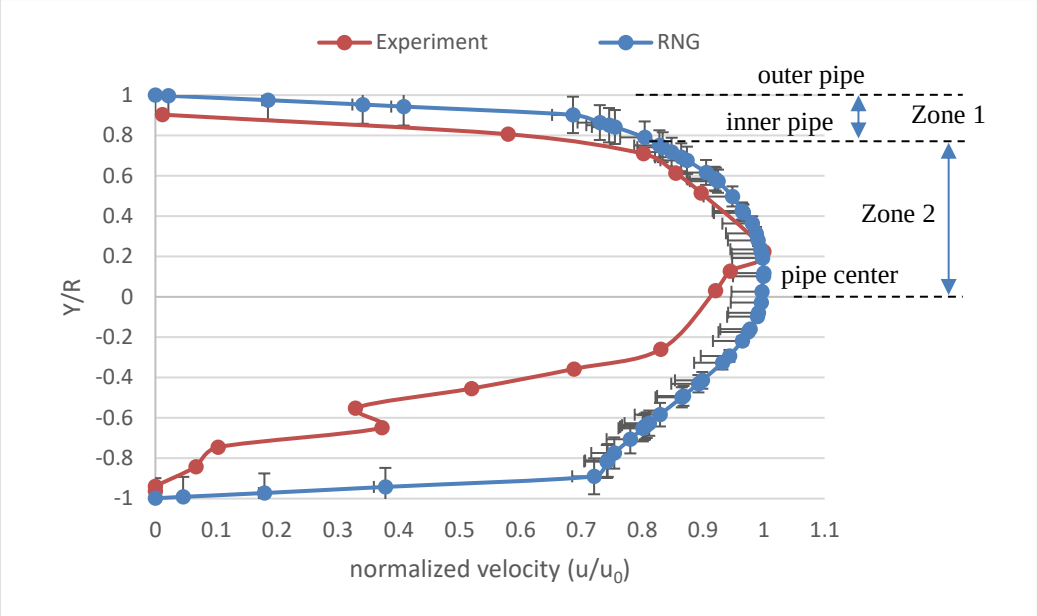

Figure 26. normalized velocity profile of slurry flow in the inner pipe at 1 m from the inlet.

The RNG k-ε model simulation at boundary conditions of 150kPa yielded a maximum mixture velocity of about 0.45 m/s. As depicted in figure 27, the acquired velocity values indicated that the slurry flow is in the range of the settling velocity of suspended solid particles. Hence, further comprehensive numerical simulations were performed with an increased pressure and velocity. While the experimental method was not used further due to the acrylic pipe cannot withstand more pressure than this limit.

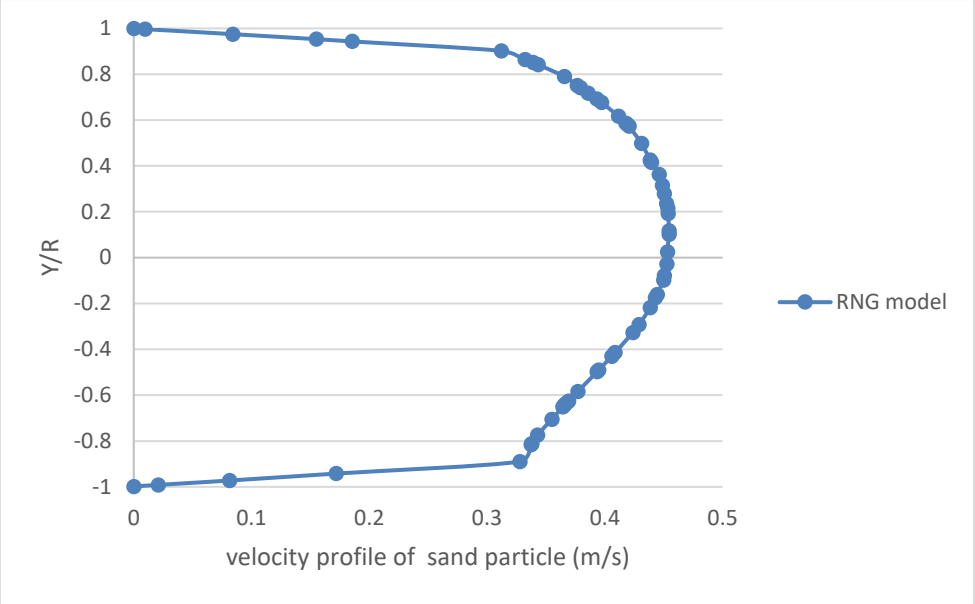

Figure 27. velocity profile of slurry flow in the inner pipe at a boundary condition of 150 Kpa.

4.3 Comprehensive simulation results and discussion:

This This section shows the effect of varying the slurry velocity on the slurry pressure drop and concentration profile. The velocity profiles of sand particles are shown at the four perforated gun holes located on the Cartesian (Y+, Y-, Z+, Z-). As depicted in figure 21, each letter indicates the Cartesian location of the gun hole on the inner pipe. Y+ hole is located at the upper slot and it is opposite to the Y- gun hole. Similarly, the location of the Z+ and Z- holes located opposite at the centerline.

4.3.1 Pressure gradient

Figure 28 depicts the change in pressure gradient of the slurry components across various slurry velocity. When increasing the slurry velocity, the term of difference in pressure between the perforated holes and the inlet pressure, located 1.7 m away, increases in agreement with previous research [62]. In figure 28, it can be observed that the pressure drop increased rapidly after the slurry velocity exceeded 4

m/s. The graph also captured the difference in the pressure drop profile for the mixture water phase, sand phase and the slurry. Ignoring the variation of the pressure drop between the phases may lead to many challenges during to hydrofracturing process. The four perforated gun holes have similar pressure drop with a variance less than 0.012%. This small difference in pressure drop was most noticeable between the gun holes located at (Y+) and (Y-).

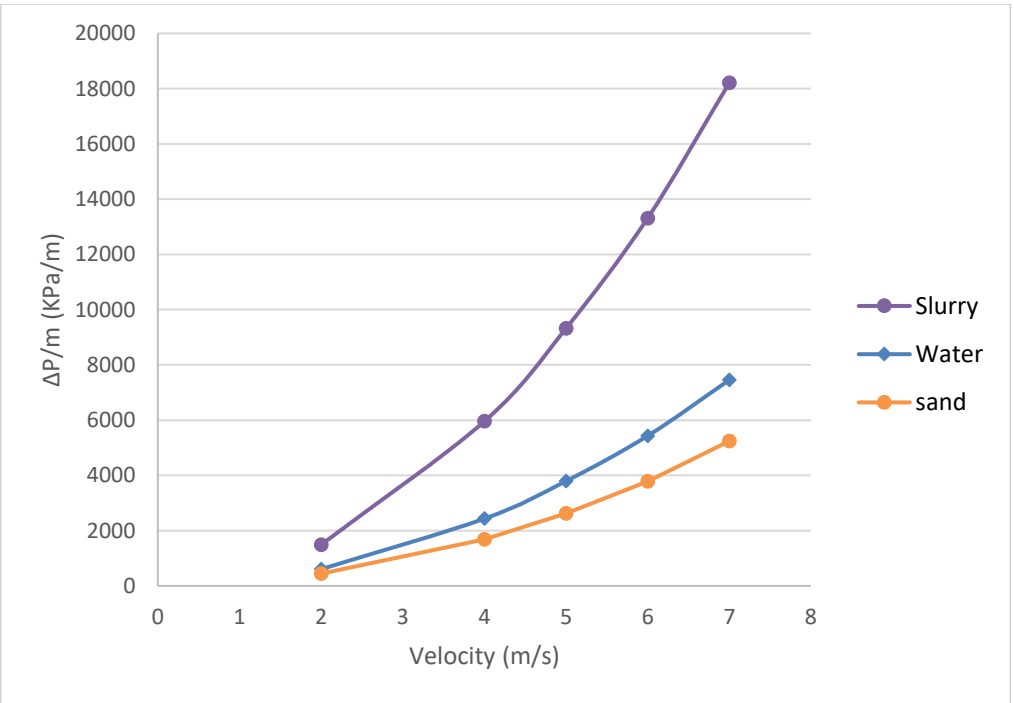

Figure 28. Simulation result of average pressure drops for different flow velocities at the perforated holes outlet.

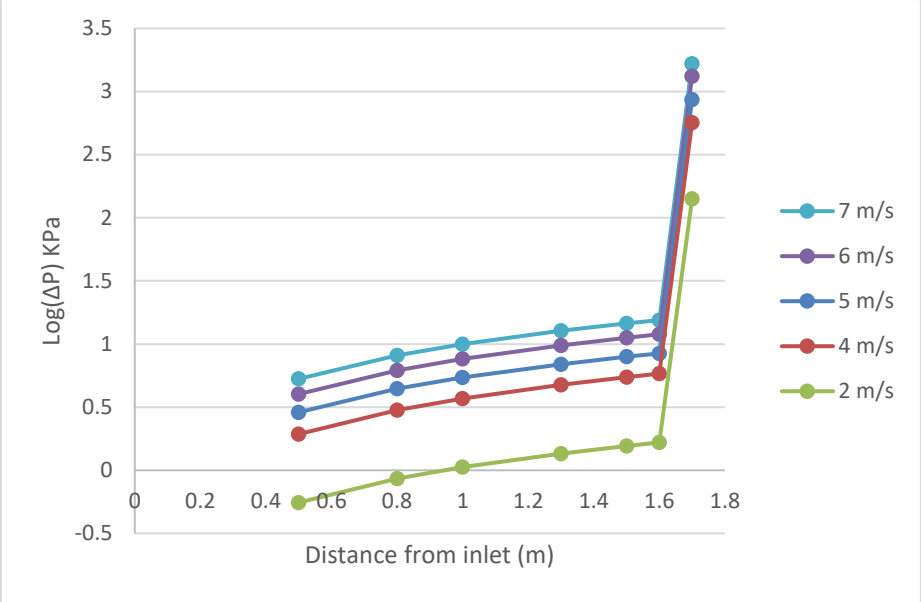

Figure 29. Logarithm of pressure drops along the horizontal axis of the inner pipe with different slurry velocities.

Figure 29 shows the pressure drop along the length of the pipe at different slurry velocities. It is clear that the logarithmic differential pressure increased gradually along the length of the pipe. At a distance of 1.7 meter along the pipe length, the slurry log(ΔP) value increased significantly, due to the presence of the perforated gun holes. The log(ΔP) value pattern was similar for the other velocities of the slurry.

As illustrated in figure 30, the higher the solid particle volume fraction in the liquid phase, the greater the differential pressure due to the momentum interaction between the liquid and the solid particles. This increased friction is attributed to the increased interactions between particles-walls, particles-liquid, and particles-particles. At 6 m/s of mixture flow, the sand particles were fully suspended. As a result, the pressure drop of the four perforated holes (Y+, Y-, Z+, Z-) slightly vary for both sand and water phases. The pressure drop across the four gun holes was almost the same

for the slurry flow. Additionally, it was possible to calculate the pressure drop separately for the water and solid phase, since Eulerian equation calculates each phase in a segregated method. Whereas, it is obvious that the pressure drop of sand and water flow is much less than the actual pressure drop of the slurry.

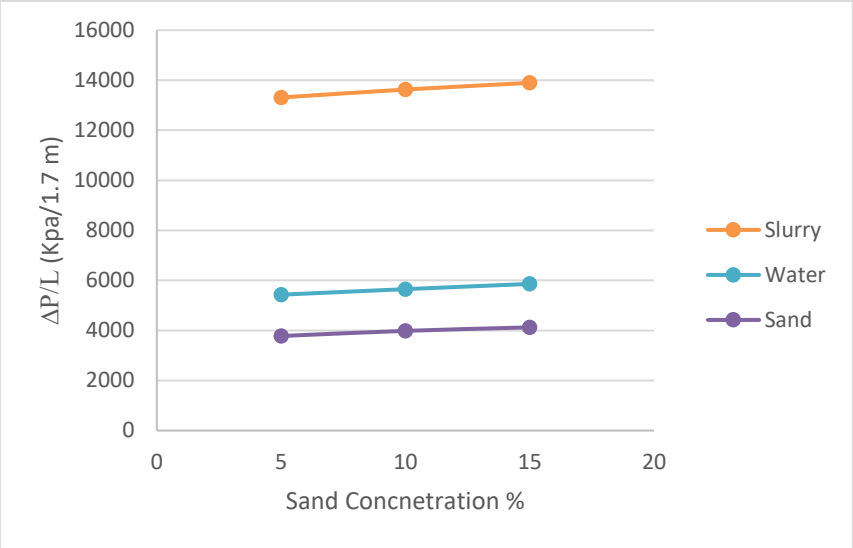

Figure 30. Comparison between the pressure drop of slurry, sand and water flow at three different concentrations (5%, 10%, and 15%) with a constant inlet velocity of 6 m/s.

4.3.2 Particle concentration:

This section shows the particle concentration profile in the radial direction at the horizontal pipe centerline for various slurry flow rates and different volume fraction of sand particles.

Figure 31 shows the concentration profile at 1.7 m from the pipe inlet for 5% volume fraction of sand particles for 5 different velocities. The results demonstrate a

broad spectrum of fluid turbulence effects on particle suspension. At low flow velocity of 2 m/s, the sand particles tend to form a moving bed layer at the bottom of the pipe. It is noticeable that the variance between sand volumetric concentration at the bottom and the top of the pipe decreases as the slurry flow rate increases. This behavior agreed with several previous studies [69], where at high flow velocities, the solid particles will be suspended by turbulence as illustrated earlier in chapter 2.

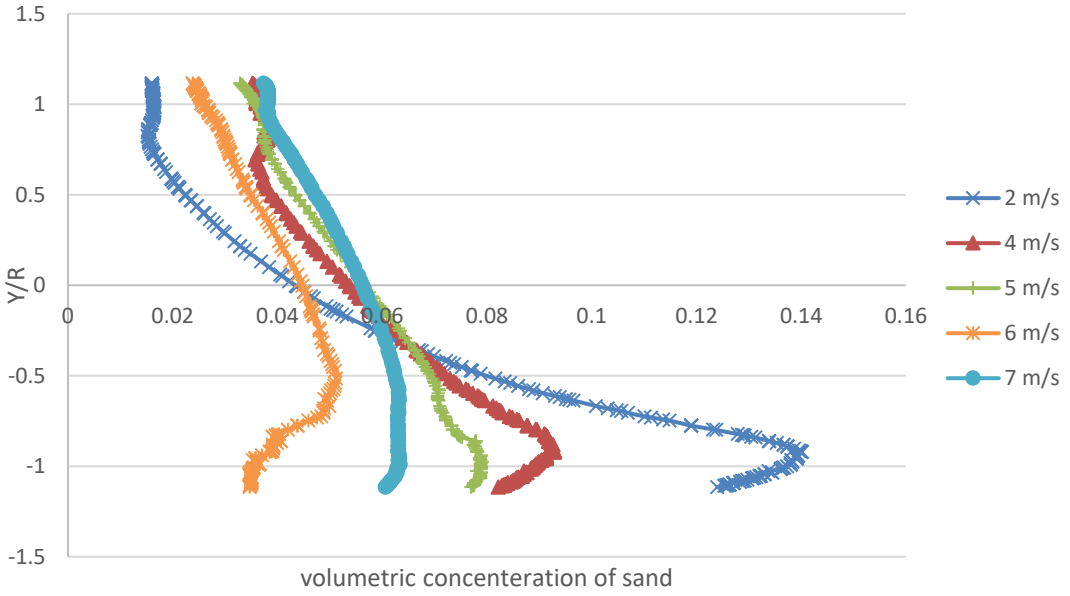

Figure 31. Volumetric sand concentration profile across vertical center line of 1.7 meter from the pipe inlet at different mixture velocities.

Figure 32 illustrates the difference in sand average concentration between the four perforated gun holes at different velocities of 5% slurry volume fraction. It is obvious that there is a high consistency in concentration profile for the slurry velocity at 6 and 7 m/s. At low flow velocities corresponding to low flow rates, the

gravitational force effect dominated the sand particles dynamic behavior. A flow of low velocity allows for the settling of sand particles at the perforated holes. Thus, increasing the possibility of screen-out and eventually blocking the gun holes during the well stimulation process. The standard-deviation of the volumetric concentration of sand particles between the four holes becomes less than 1% after the slurry velocity exceeds 6 m/s, while at a slurry velocity of 2 m/s, the standard deviation was about 3.7%.

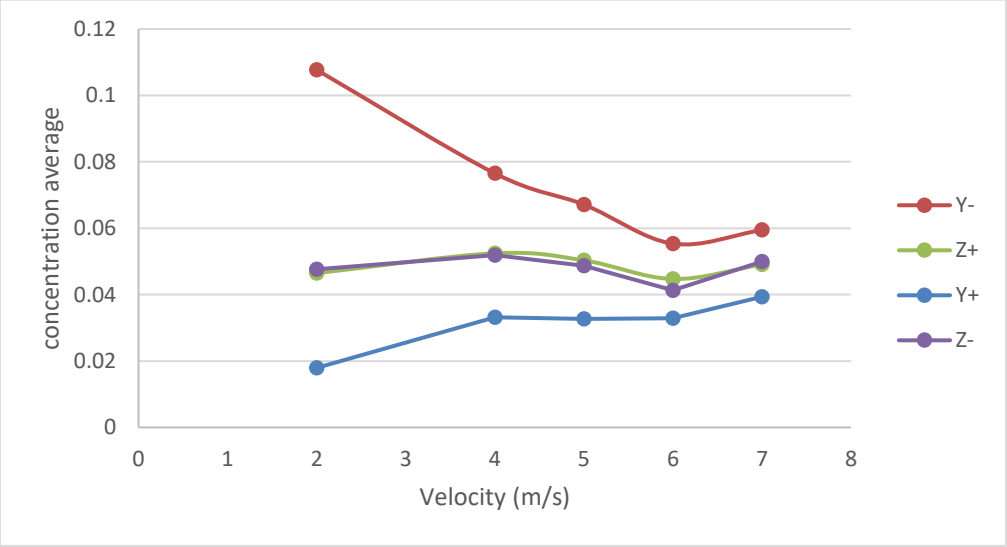

Figure 32. Volumetric concentration average at the four perforated holes of 5% slurry volume fraction with different velocities.

Figure 33 depicts the concentration profiles of three different sand volume fractions of 5%, 10%, and 15%, at slurry inlet velocity of 6 m/s. Although the slurry velocity is higher than the settling velocity of slurry flow at 5% concentration, the sand particles tend to become less consistent along the radial direction as the volumetric concentration increases. The interaction of the sand particles and the pipe

internal wall increases at higher volumetric concentration. Figure 34, shows the standard deviation of the three-phase fractions for the four perforated holes at a mixture flow rate of 6m/s. At the lowest sand volume fraction of 5%, the concentration difference between the holes was less than 1% and reaching about 2% in the other volume fraction of 10% and 15%. The standard-deviation of particle concentration decreased at mixture of 15% volume fraction. This phenomenon was observed by Ofei and Ismaile (2016), where they emphasized that a large increase of sand concentration may lead to an increase of the sand particles bonding. Hence, suspending the particle concentration in almost the entire pipe [68].

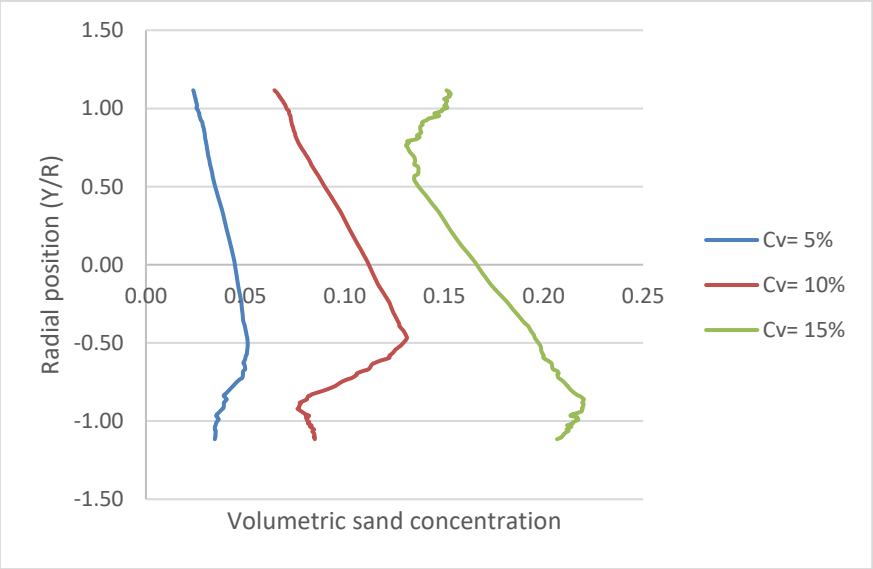

Figure 33. Concentration profile of three different sand volume fractions at slurry inlet velocity of 6 m/s.

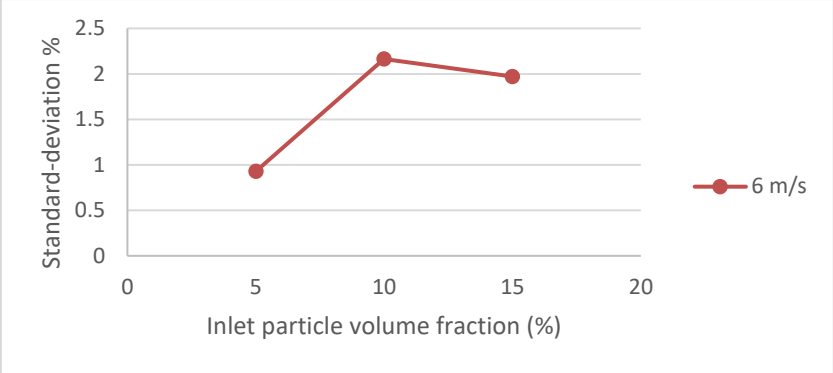

Figure 34: Standard deviation of concentration profile of different sand volume fractions at 6 m/s.

4.3.3 Velocity distribution:

Figures 35 to 39 show the velocity contours of the sand solid particles at Y+ and Y- of the perforated holes at five different inlet flow velocity. For the five cases, the difference of the maximum velocity of solid particles between Y+ and Y- of the perforated holes did not exceed 0.95 m/s. The velocity contours showed very near symmetric profile at the perforated holes with maxima depicted at the center of the holes. Where, the flow is constricted into the vena contracta region (the midsection of the hole). While, the velocity near the sharp edge of the holes is almost zero. This because the fluid cannot make sharp 90^{O} turns easily, especially at high velocity, in addition to the swirling turbulent eddies generated at the edges of the perforated holes. This result is supported by previous study [82]. Figure 40 depicts the linear relationship between the slurry velocity and the sand particle velocity calculated at the outlet of the perforated gun holes. The correlation of sand particles velocity at the inlet and the outlet is equal 30.731. That means that the maximum outlet velocity of the 5 mm diameter gun hole is about 30 times higher than the slurry inlet velocity.

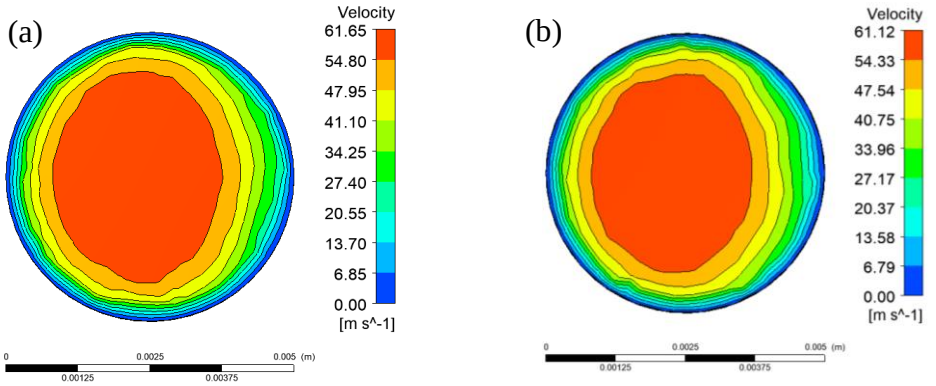

Figure 35. Contour plot of velocity distribution of the outlet perforated holes: a) Y+ b) Y- at boundary inlet condition of 2 m/s.

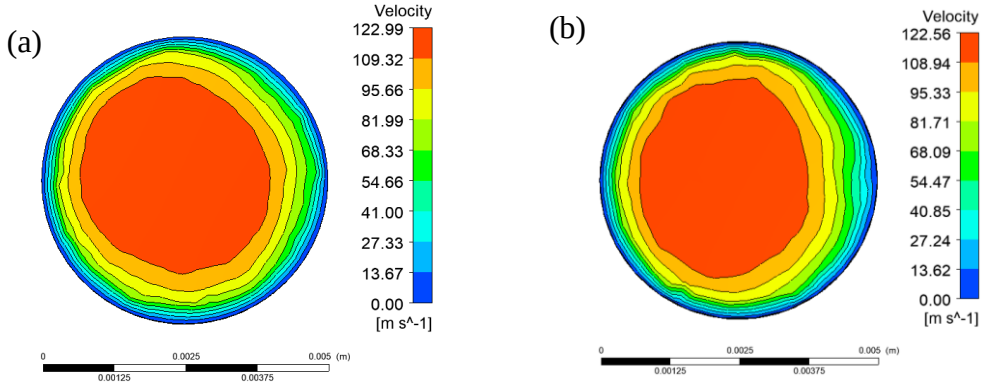

Figure 36. Contour plot of velocity distribution of the outlet perforated holes: a) Y+ b) Y- at boundary inlet condition of 4 m/s.

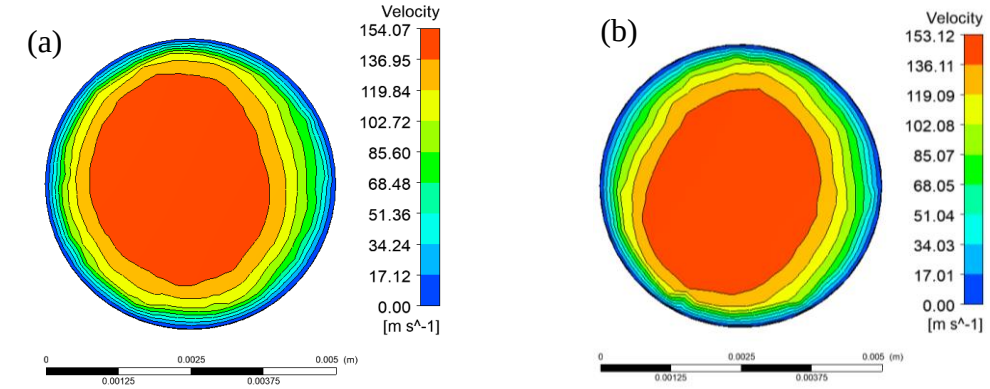

Figure 37. Contour plot of velocity distribution of the outlet perforated holes: a) Y+ b) Y- at boundary inlet condition of 5 m/s.

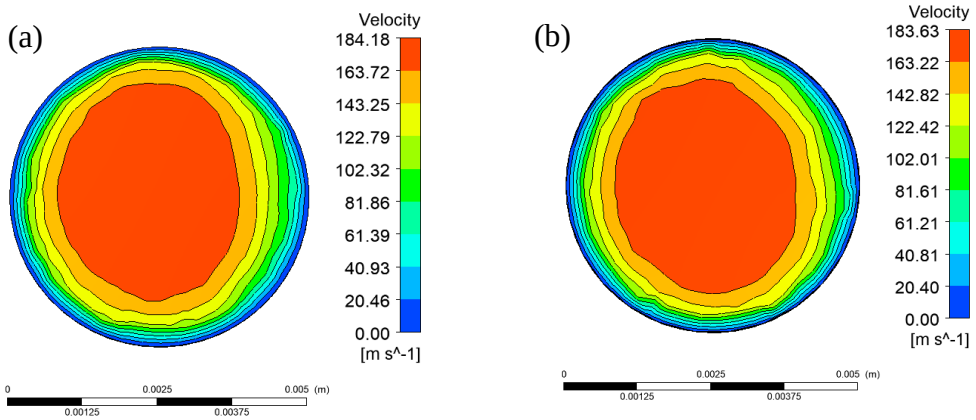

Figure 38. Contour plot of velocity distribution of the outlet perforated holes: a) Y+ b) Y- at boundary inlet condition of 6 m/s.

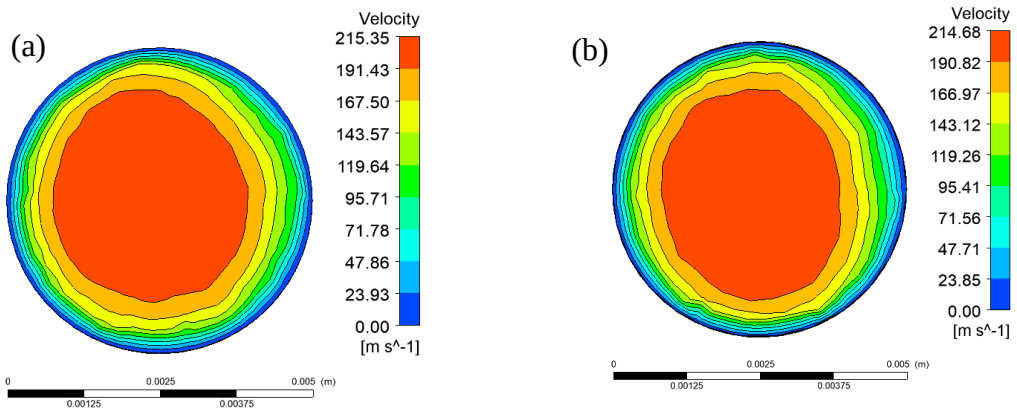

Figure 39. Contour plot of velocity distribution of the outlet perforated holes: a) Y+ b) Y- at boundary inlet condition of 7 m/s.

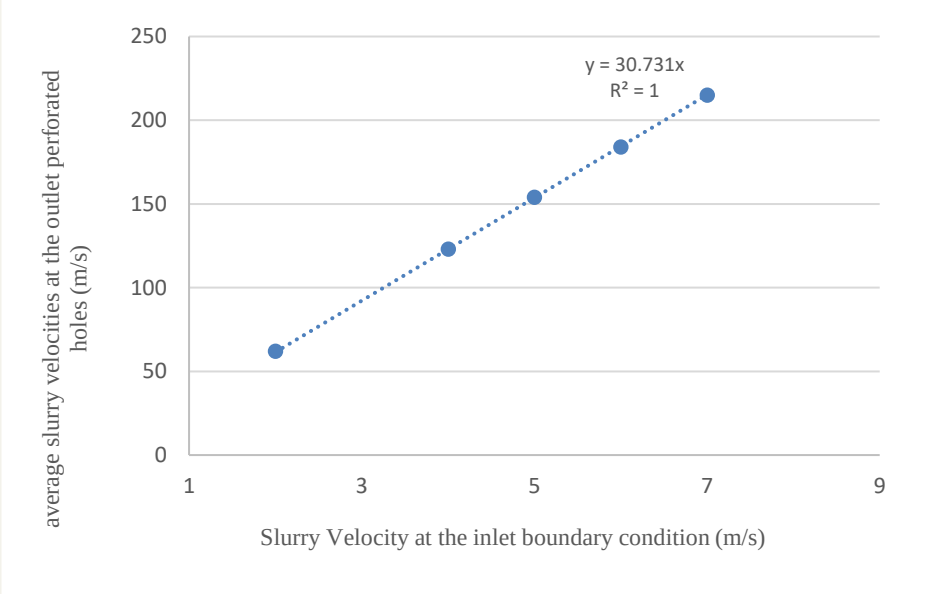

Figure 40. Correlation between the inlet velocity and the average velocities at the outlet perforated holes for the slurry system.

Figure 41 illustrates the correlation between the slurry inlet velocity and the pressure calculated at the outlet perforated holes. Where, an empirical equation of second order non-linear relationship is generated. The empirical equation could be

used to calculate the hydrofracturing pressure of the slurry flow at the perforated holes outlet while, taking into account the geometry and the boundary condition under which this simulation was made. Furthermore, it is imperative to indicate that the pressure variance between the four perforated holes is not significant, however, the sand particle concentration variance between the perforated holes is critical as explained in figure 32. The generated hydrofracturing pressure is in agreement with similar research [83].

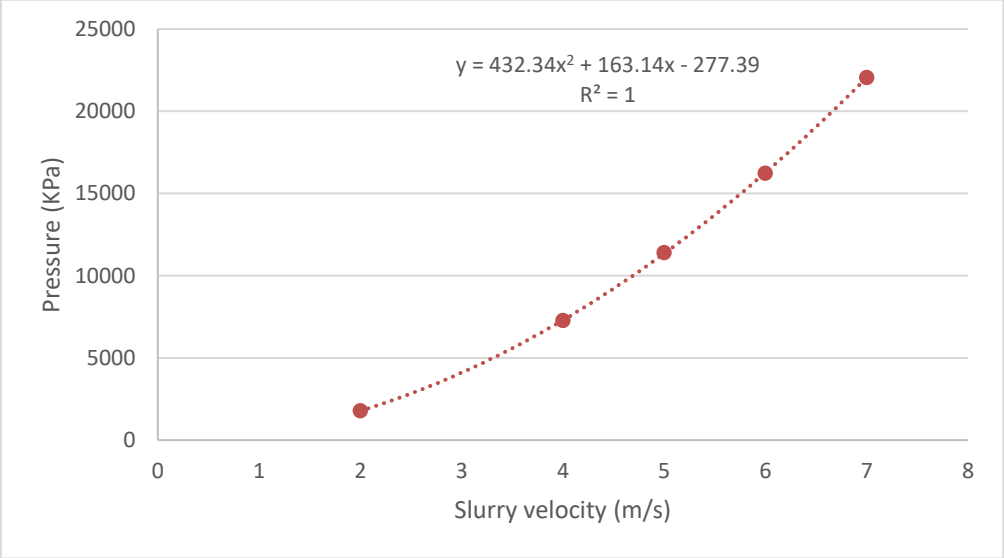

Figure 41. Correlation between the slurry inlet velocity and the pressure at the outlet perforated holes for the slurry system.

CHAPTER 5: CONCLUSION

During the process of well stimulation, hydraulic fracturing occurs when the pressure of the fluid injected into a formation is sufficient to generate forces exceed the tensile strength of the rock. Failure of the rock allows fractures to propagate along the path of least resistance. To design a successful hydraulic fracturing treatment for horizontal wells, accurate information on the transport properties of slurry in a horizontal pipe is vital. This paper presented a comprehensive numerical and experimental study of hydrofracturing slurry flow in a horizontal pipe. The results acquired from a laboratory scale experiment was used to assess the CFD numerical results. Through numerical and experimental investigation, the RNG k- ε turbulence closure model is characterized to be the more suited model to use in slurry flows simulation in horizontal pipes over the standard k- ε and RSM models. Using three different volumetric sand concentrations and five different slurry inlet velocities, the RNG k- ε model successfully captured the flow behavior of flow phases. For further analysis, the RNG k- ε model was used to analyze the turbulent slurry flow in the perforated pipe. The commercial CFD ANSYS-Fluent software was used to numerically solve and analyze the two-phase (sand-water) slurry flow through a 50.8 mm diameter horizontal pipe with different perforated holes. Using the RNG k- ε model, a simulation was carried for a slurry flow velocity range of 2-7 m/s with 5% efflux concentration and one sand particles size of 500 μm of a density of 1442 kg/m3. More simulations were carried using three efflux concentrations of 5%, 10%, and 15% at a slurry inlet velocity of 6 m/s. The novelty of this paper lies on presention of the relationship between the slurry flow velocity at the inlet and the average slurry flow at the outlet of the perforated gun holes in a horizontal pipe. The results of the thesis are concluded in the following points:

1- Inaccurate predictions of frictional pressure losses and settling conditions for the transportation of drilling fluids in the annuli can lead to a number of costly drilling problems such as screen-out and pumping flow rate.
2- Water and sand slurry flow are the most popular fracturing fluid through the history due to their availability and low unit cost.
3- The analysis of pressure drop and solid concentration at the outlet perforated holes enhanced the selection of slurry and mixture velocity during the operation.
4- Literature Review showed the novelty of this thesis, as none of the researchers have studied nor analyzed the slurry flow at the outlet perforated holes in a horizontal pipe.
5- The (RNG) k-ε model deemed to be the best matching turbulence model in capturing the slurry flow behavior. The RNG k- ε model obtained results were in agreement with the experimental results better than the RSM or standard k-ε model counterparts. This result infers that the RNG K- ε model is a more suited model for the slurry flow analysis.
6- The numerical results showed that the pressure drop of the perforated gun holes increases rapidly after the slurry velocity exceeds 4 m/s.
7- During hydrofracturing process, a slurry high flow rate is required to mitigate against screen out or blocking of the gun holes.
8- A linear relationship between the surly velocity and the sand solid phase velocity was established. The correlation of sand particles velocity at the inlet and the outlet is equal 30.731.

9- An empirical equation of a nonlinear relationship between the hydrofracturing pressure at the perforated holes outlet and the slurry inlet velocity was established.

For future work, improvements in the current thesis can be concluded in the following points:

- Performing the slurry flow experiment with higher velocities and larger lab-scale.
- Testing different diameters of sand particles with a wider range of concentrations.
- Develop an empirical model that can calculate the slurry flow pressure drops at the outlet perforated holes.
- Investigate different diameters of perforated holes at different concentrations.

REFERENCES

[1] Osiptsov, A. A. (2017). Fluid Mechanics of Hydraulic Fracturing: a Review. *Journal of Petroleum Science and Engineering*, 513-535.

[2] Speight, J. G. (2017). Chapter Five - Hydraulic Fracturing. In *Deep Shale Oil and Gas* (pp. 209-260). Laramie: CD&W Inc.

[3] Troy Cook, J. P. (2018, January 30). *Hydraulically fractured horizontal wells account for most new oil and natural gas wells*. Retrieved from U.S. Energy Information Administration: https://www.eia.gov/todayinenergy/detail.php?id=34732#

[4] Chilingarian, G., Jr, J. R., & Kumar, S. (2008). Chapter 4 Fracturing. In G. Chilingarian, J. R. Jr, & S. Kumar, *Surface Operations in Petroleum Production, II* (pp. 101-159). Elsevier.

[5] Chen, X., Li, Y., Zhao, J., Xu, W., & Fu, D. (2018). Numerical investigation for simultaneous growth of hydraulic fractures in multiple horizontal wells. Journal of Natural Gas Science and Engineering, 44-52.

[6] Leggett, M. (2011, Jul 16). *Hydraulic fracturing and shale gas*. Retrieved from earthtimes: http://www.earthtimes.org/encyclopaedia/environmental-issues/hydraulic-fracturing-shale-gas/

[7] Eftekharia, B., Mardera, M., & Patzekb, T. W. (2018). Field data provide estimates of effective permeability, fracture spacing, well drainage area and incremental production in gas shales. Journal of Natural Gas Science and Engineering, 141-151.

[8] Suri, Y., Islam, S. Z., & Hossain, M. (2019). A new CFD approach for proppant transport in unconventional hydraulic fractures. Journal of Natural Gas Science and Engineering.

[9] Gong, Y., Mehana, M., El-Monier, I., & Viswanathan, H. (2020). Proppant placement in complex fracture geometries: A computational fluid dynamics study. Journal of Natural Gas Science and Engineering, 103295.

[10] Lawn, C., & Gluyas, J. (2018). Novel energy sources and carbon sinks underground. *Journal of Power and Energy*, 3-5.

[11] Lash, G. G., & Lash, E. P. (2014). Early History of the Natural Gas Industry. *AAPG Annual Convention and Exhibition.* Fredonia.

[12] Morton, M. Q. (2013). Unlocking the Earth - A Short History of Hydraulic Fracturing. *Vol. 10, No. 6* .

[13] ROBERTS, E. A. (1866). *NEW YORK Patent No. 59936.*

[14] Campos, de, V. P., Labat, G. A., Sansone, E., Gouvea, D., & Silva, G. F. (2018). Development of Sodium Hydroxide-Activated Metakaolin with Nanocarbon Materials as Synthetic Ceramic Proppants. *Materials Science Forum, vol. 912* (pp. 251-256). Trans Tech Publications.

[15] Montgomery, C. T., & Smith, M. B. (2010). Hydraulic Fracturing: History of an Enduring Technology. *Journal of Petroleum Technology*, 26-40.

[16] Hydraulic Fracturing: History of an Enduring Technology. (2010). *Journal of Petroleum Technology*, 26 - 40.

[17] Clark, J. B. (1949). A HYDRAULIC PROCESS FOR INCREASING THE PRODUCTIVITY OF WELLS . *Journal of Petroleum Technology*, 1-8.

[18] Holditch, S. A. (2006). Chapter 8 - Hydraulic Fracturing. In L. W. Lake, *Petroleum Engineering Handbook* (pp. 323-366). Holditch: Society of Petroleum Engineers.

[19] Rahmaniana, M., & Kantzas, A. (2018). Stochastic generation of virtual porous media using a pseudo-crystallization approach. *Journal of Natural Gas Science and Engineering*, 204-217.

[20] Ahmed, S. U., & Mohanty, S. (2018). Numerical Analysis of Slurry Flow Characteristics through Horizontal Pipeline using CFD. *International Research Journal of Engineering and Technology*, 1348-1354.

[21] Shah, S. (1993). Rheological Characterization of Hydraulic Fracturing Slurries. *Society of Petroleum Engineers*, 123-130.

[22] Bohloli, B., & Pater, C. d. (2006). Experimental study on hydraulic fracturing of soft rocks: Influence of fluid rheology and confining stress. *Journal of Petroleum Science and Engineering*, 1-12.

[23] Munson, B. R., Young, D. F., & Okiishi, T. H. (2002). *Fundamentals of Fluid Mechanics.* New York: John Wiley & Sons.

[24] Anon. (2010). *Centrifugal Pump Handbook.* Sulzer Pumps Ltd.

[25] Wasp, E. J., Kenny, J. P., & Gandhi, R. L. (1977). *Solid-Liquid Flow – Slurry Pipeline Transport. Series on Bulk Materials Handling Vol. 1.* Clausthal: Trans Tech Publications.

[26] Abulnaga, B. (2002). *Slurry systems handbook.* New York: McGraw-Hill Handbooks.

[27] Bootle, M. J. (2002). Selection and Sizing of Slurry Pumps. In *Mineral Processing Plant Design, Practice, and Control.* (pp. 1373-1402). Colorado: Society of Mining Engineers.

[28] Reynolds, O. (1883). An experimental investigation of the circumstances which determine whether the motion of water shall be direct or sinuous, and of the law of resistance in parallel channels. *Philosophical Transactions of the Royal Society*, 935-982.

[29] Bird, R., Stewart, W., & Lightfoot, E. (2002). *Transport Phenomena", Second edition.* London: John Wiley.

[30] Durand, R., & Condolios, E. (1952). Experimental investigation of the transport of solids in. *Paper presented at the Deuxieme Journée de l'hydraulique*. Societé Hydrotechnique de France.

[31] Anon. (2009). *Slurry Pump Handbook, 5th edition.* Weir Slurry Group, Inc.

[32] Grzina, A. T., Roudnev, A., & Burgess, K. E. (2002). *SLURRY PUMPING MANUAL*. WARMAN INTERNATIONAL LTD and EnviroTech Pumpsystems.

[33] Carleton, A. J., & Cheng, D. C.-H. (1974). Design velocities for hydraulic conveying of settling suspensions. *Proceedings of Hydrotransport 3, the third international conference on the hydraulic transport of solids in pipes*, (pp. 57-74). Colorado.

[34] Wilson, K. C., Addie, G. R., Sellgren, A., & Clift, R. (2006). *Slurry Transport Using Centrifugal Pumps, 3rd edition.* New York: Springer Science+Business Media Inc.

[35] O'Brien, M. (1933). Review of the theory of turbulent flow and its relations to sediment transport. *Transaction of the American Geophysical Union*, 487-491.

[36] Rouse, H. (1937). Modern conceptions of the mechanics of fluid turbulence. *Transactions of ASCE*, 463-505.

[37] Shook, C., & Daniel, S. (1965). Flow of suspensions of solids in pipeline: I. Flow with a stable stationary deposit. *The Canadian Journal of Chemical Engineering*, 56-72.

[38] Karabelas, A. (1977). Vertical distribution of dilute suspensions in turbulent pipe flow. *AIChE Journal*, 426-434.

[39] Shook, C., Daniel, S., Scott, J., & Holgate, J. (1968). Flow of suspensions in pipelines. *The Canadian Journal of Chemical Engineering*, 238-244.

[40] Gillies, R., Shook, C., & Wilson, K. (1991). An improved two layer model for horizontal slurry pipeline flow. *The Canadian Journal of Chemical Engineering*, 173–178.

[41] Roco, M., & Shook, C. (1983). Modeling of slurry flow: The effect of particle size. *The Canadian Journal of Chemical Engineering*, 494–503.

[42] Gillies, R. G., & Shook, C. A. (1994). CONCENTRATION DISTRIBUTIONS OF SAND SLURRIES IN HORIZONTAL PIPE FLOW. *Particulate Science and Technology: An International Journal*, 45-69.

[43] Seshadri, V., Malhotra, R., & Sundar, K. (1982). Concentration and size distribution of solids in a slurry pipeline. *In: Proc. 11th Nat. Conference on Fluid mechanics and fluid power.* Hyderabad.: B.H.E.L.

[44] Roco, M., & Shook, C. (1984). Computational methods for coal slurry pipeline with heterogeneous size distribution. *Powder Technology*, 159-176.

[45] Gillies, R., Hill, K., Mckibben, M., & Shook, C. (1999). Solids transport by laminar Newtonian flows. *Powder Technology*, 269-277.

[46] Gillies, R., & Shook, C. (2000). Modeling high concentration settling slurry flows. *The Canadian Journal of Chemical Engineering*, 709-716.

[47] Wasp, E., Aude, T., Kenny, J., Seiter, R., & Jacques, R. (1970). Deposition velocities, transition velocities and spatial distribution of solids in slurry pipelines. *the 1st International British Hydromechanics Research Association Hydraulic Transport of Solids in Pipes Conference* (pp. 53-76). Coventry: BHRA Fluid Engineering.

[48] Doron, P., Granica, D., & Barnea, D. (1987). Slurry flow in horizontal pipes—experimental and modeling. *International Journal of Multiphase Flow*, 535-547.

[49] Sundqvist, A., Sellgren, A., & Addie, G. (1996). Slurry pipeline friction losses for coarse and high density products. *Powder Technology*, 19-28.

[50] Ghanta, K., & Purohit, N. (1999). Pressure drop prediction in hydraulic transport of bi-dispersed particles of coal and copper ore in pipeline. *The Canadian Journal of Chemical Engineering*, 127-131.

[51] Mishra, R., Singh, S., & Seshadri, V. (1998). Improved model for prediction of pressure drop and velocity field in multisized particulate slurry flow through horizontal pipes. *Powder Handling and Processing Journal*, 279-289.

[52] Wilson, K., Clift, R., & Sellgren, A. (2002). Operating points for pipelines carrying concentrated heterogeneous slurries. *Powder Technology*, 19-24.

[53] Toda, M., Shimazaki, K., & Maeda, S. (1972). Hydraulic conveying of solids through pipe bends. *Journal of Chemical Engineering of Japan*, 4-13.

[54] Turian, R. M., & Yuan, T. F. (1977). Flow of slurries in pipelines. *AIChE Journal*, 232-243.

[55] Geldart, D., & Ling, S. J. (1990). ense phase conveying of fine coal at high total pressures. *Powder Technology*, 243-252.

[56] Doron, P., & Barnea, D. (1995). Pressure drop and limit deposit velocity for solid-liquid flow in pipes. *Chemical engineering science*, 1595-1604.

[57] Mukhtar, A., Singh, S. N., & & Seshadri, V. (1995). Pressure drop in a long radius 90° horizontal bend for the flow of multisized heterogeneous slurries. *International journal of multiphase flow*, 329-334.

[58] Turian, R. M., Ma, T. W., Hsu, F. L., & Sung, D. J. (1998). Flow of concentrated non-Newtonian slurries: 1. Friction losses in laminar, turbulent and transition flow through straight pipe. *International journal of Multiphase flow*, 225-242.

[59] Bellas, J., Chaer, I., & Tassou, S. A. (2002). Heat transfer and pressure drop of ice slurries in plate heat exchangers. *Applied Thermal Engineering*, 721-732.

[60] Matousek, V. (2001). Pressure drops and flow patterns in sand-mixture pipes. *Experimental Thermal and Fluid Science*, 693-702.

[61] Kaushal, D., & Tomita, Y. (2002). Solids concentration profiles and pressure drop in pipeline flow of multisized particulate slurries. *International Journal of Multiphase Flow*, 1697-1717.

[62] Ling, J., Skudarnov, P., Lin, C., & Ebadian, M. (2003). Numerical investigations of liquid–solid slurry flows in a fully developed turbulent flow region. *International Journal of Heat and Fluid Flow*, 389-398.

[63] Hernández, F. H., Blanco, A. J., & Rojas-Solórzano, L. (2008). CFD MODELING OF SLURRY FLOWS IN HORIZONTAL PIPES. *8th Symposium on Applications in Computational Fluid Dynamics* . Jacksonville: ASME.

[64] Kaushal, D., Thinglas, T., Tomita, Y., Kuchii, S., & Tsukamoto, H. (2012). CFD modeling for pipeline flow of fine particles at high concentration. *International Journal of Multiphase Flow*, 85-100.

[65] Vlask, P., Kysela, B., & Chara, Z. (2012). FLOW STRUCTURE OF COARSE-GRAINED SLURRY IN A HORIZONTAL PIPE. *Journal of Hydrology and Hydromechanics*, 115-124.

[66] Nabil, T., El-Sawaf, I., & El-Nahhas, K. (2013). COMPUTATIONAL FLUID DYNAMICS SIMULATION OF THE SOLIDLIQUID SLURRY FLOW IN A PIPELINE. *International Water Technology Conference*, (pp. 5-7). Istanbul.

[67] Gopaliya, M. K., & D.R., K. (2016). Modeling of sand-water slurry flow through horizontal pipe using CFD. *Journal of Hydrology and Hydromechanics*, 261-271.

[68] Ofei, T. N., & Ismail, A. Y. (2016). Eulerian-Eulerian Simulation of Particle-Liquid Slurry Flow in Horizontal Pipe. *Journal of Petroleum Engineering*, 10.

[69] Sultan, R. A., Rahmana, M. A., Zendehboudia, S., Talimi, V., & Kelessidis, V. C. (2018). Sensitivity analysis of a CFD model for simulating slurry flow through pipline. *Journal of Nature Science and Sustainable Technology*.

[70] Skudarnov, P. V., Lin, C. X., & Ebadian, M. A. (2004). Double-Species Slurry Flow in a Horizontal Pipeline. *Journal of Fluids Engineering*, 125-131.

[71] Aroussi, A., Abdul Ghani, S., and Rice, E., "PIV Measurement and Numerical Simulation of Airflow Field in a Road Vehicle HVAC Cowl Box," SAE Technical Paper 2001-01-0294, 2001, https://doi.org/10.4271/2001-01-0294.

[72] Hansen, B. (2013, March 05). *Casing Perforating Overview.* Retrieved from Devon Energy Corporation: https://www.epa.gov/sites/production/files/documents/casingperforatedoverview.pdf

[73] Huang, Z., Guo, B., Shaibu, R., (2020). Lab-Supported Hypothesis and Mathematical Modeling of Crack Development in the Fluid-Soaking Process of Multi-Fractured Horizontal Wells in Shale Gas Reservoirs, Energies, volume 13, https://doi.org/10.3390/en13051035.

[74] Ghani, S., Gamaledin, S. M. A., Bakochristou, F., El-Bialy, E., Mohamed, M. M., Elsawi, R. M. E., (2018), Numerical and wind tunnel investigation of Hot Air Recirculation across Liquefied Natural Gas Air Cooled Heat Exchangers, Journal of Wind Engineering and Industrial Aerodynamics, Volume 172, Pages 409-422, ISSN 0167-6105, DOI 10.1016/j.jweia.2017.11.026.

[75] ANSYS. (2009, 01 23). *ANSYS FLUENT 12.0 Theory Guide.* Retrieved from ANSYS: https://www.afs.enea.it/project/neptunius/docs/fluent/html/th/main_pre.htm

[76] Rodriguez, S. (2019). *Applied Computational fluid Dynamics and Turbulence Modeling.* Albuquerque: Sandia National Laboratories.

[77] Skudarnov, P.V., Kang, H.J., Lin, C.X., Ebadian, M.A., Gibbons, P.W., Erian, F.F., Rinker, M., (2001), Experimental Investigation of Single- and Double-Species Slurry Transportation in a Horizontal Pipeline. Proc. ANS 9th International Topical Meeting on Robotics and Remote Systems, Seattle, WA.

[78] Newitt, D.M., Richardson, J.F., Abbot, M., Turtle, R.B., (1955), Hydraulic conveying of solids in horizontal pipes. Transactions of the Institute of Chemical Engineers 33, 93–113.

[79] Energy. (1998). In F. Government, Code of Federal Regulations (pp. 200-499). Washington: The office of the Federal Register National Archives and Records Administration.

[80] Maxwell, S. E., & D, D. H. (2004). Designing Experiments and Analyzing Data: A Model Comparison Perspective. New York: Tayler & Francis Group.

[81] Darby, R. (2001). Chemical Engineering Fluid Mechanics. New York: Marcel Dekker.

[82] Çengel, Y. A., & Cimbala, J. M. (2006). FLOW IN PIPES. In Y. A. Çengel, & J. M. Cimbala, *FLUID MECHANICS - FUNDAMENTALS AND APPLICATIONS* (pp. 321-398). New York: McGraw-Hill.

[83] Zhang, J., & Yin, S. (2017). Fracture gradient prediction: an overview and an improved method. Petroleum Science, 720-730

Appendix A

Appendix A: Durand's limiting settling velocity graph

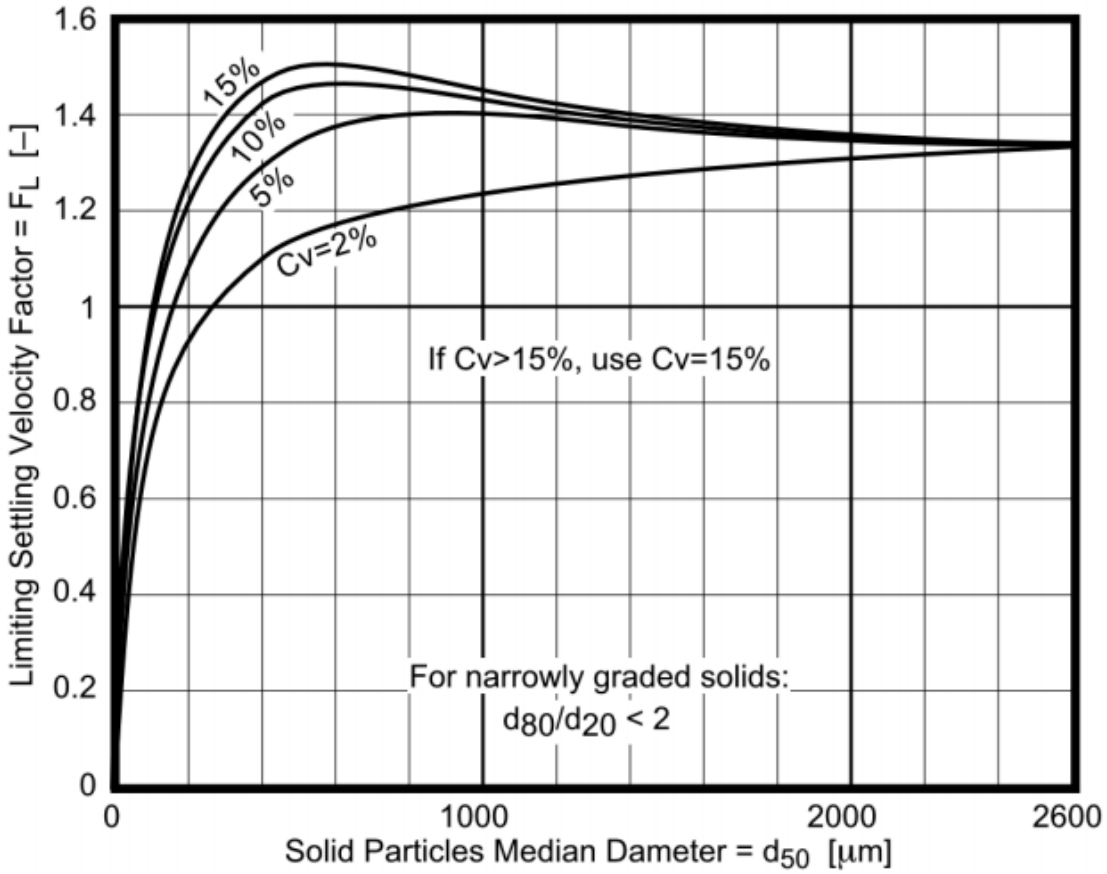

Appendix B

Appendix B: Modified Durand's limiting settling velocity graph.

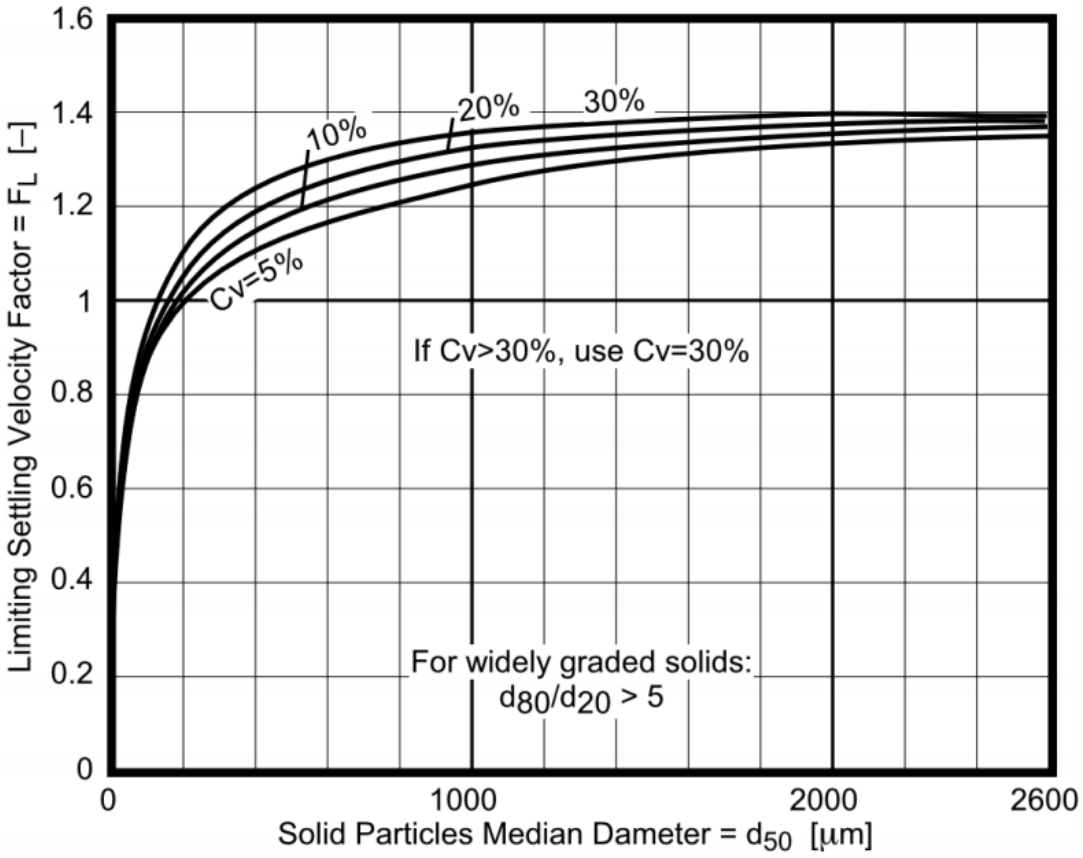

Appendix C

Appendix C: Operating characteristics at 50 Hz, 2 poles.

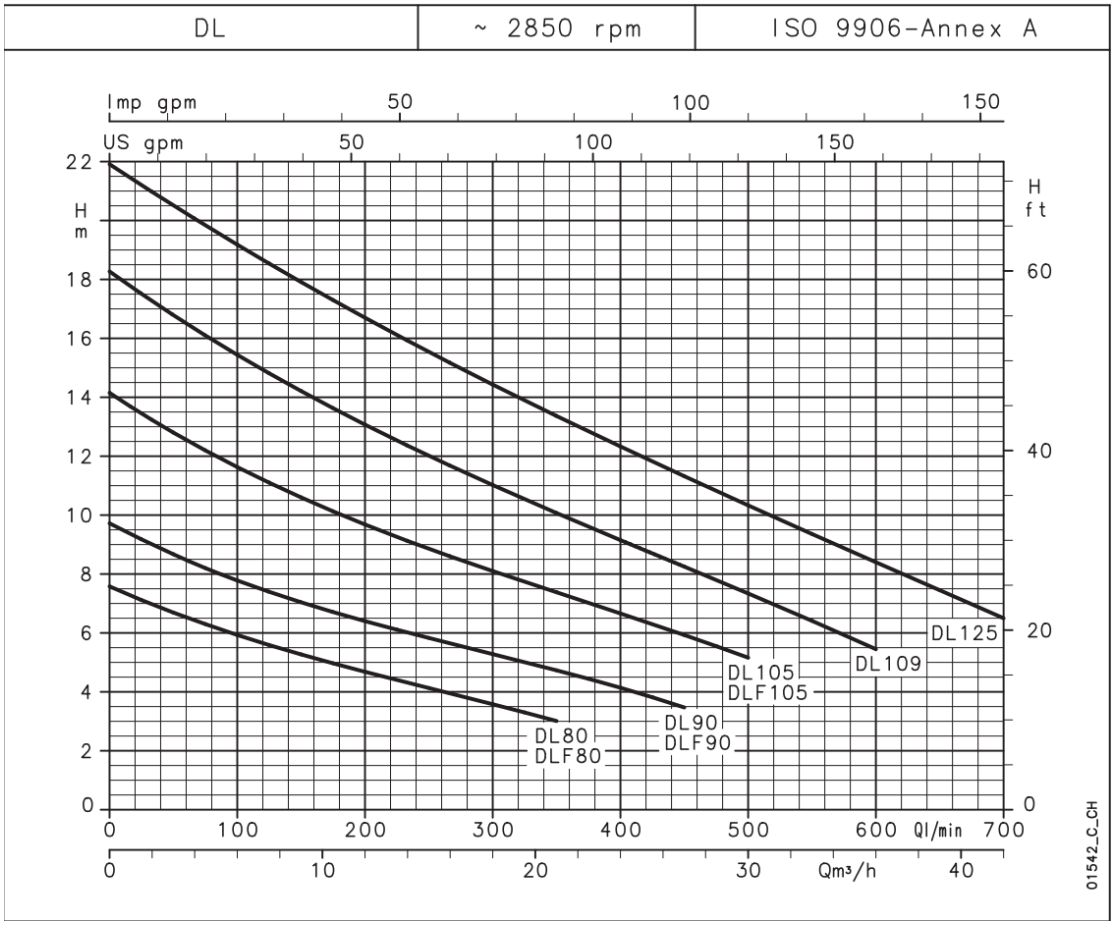

Appendix C: Hydraulic performance table.

PUMP TYPE	RATED POWER		Q = DELIVERY											
			l/min	0	100	150	200	250	300	350	400	450	500	600	700
			m³/h	0	6	9	12	15	18	21	24	27	30	36	42
	kW	HP	H = TOTAL HEAD METRES COLUMN OF WATER												
DL(M) 80-DLF(M) 80	0,6	0,8	7,6	5,9	5,3	4,7	4,1	3,6	3,0						
DL(M) 90-DLF(M) 90	0,6	0,8	9,7	7,8	7,0	6,4	5,8	5,3	4,7	4,1	3,5				
DL 105 - DLF105	1,1	1,5	14,1	11,6	10,6	9,7	8,9	8,1	7,4	6,7	5,9	5,2			
DL(M) 109	1,1	1,5	18,3	15,4	14,2	13,1	12,0	11,0	10,1	9,2	8,2	7,3	5,4		
DL 125	1,5	2	21,9	19,2	17,9	16,7	15,5	14,4	13,4	12,3	11,3	10,3	8,4	6,5	

These performances are valid for liquids with density ρ = 1,0 kg/dm³ and kinematic viscosity ν = 1 mm²/s. dl-2p50-en_b_th

Appendix D

Appendix D: Technical specification of digital sanitary pressure gauge.

2030 Series Sanitary Gauges

ASHCROFT
Trust the shield.

FEATURES

- Multi-Functional digital pressure gauge with optional 4-20mA output 1 or 2 SPDT Switches
- Large LCD display
- ±0.25% of span terminal point accuracy
- IP65 Weatherproof case
- Material Traceability Certification to EN 10204: 2004 3.1 (Excludes 2036 Series)

SPECIFICATIONS	
Accuracy:	±0.25% of span, terminal point
Process Connection:	¾" Tri-Clamp® (±0.5% of span accuracy) 1½" Tri-Clamp® 2" Tri-Clamp® 1½" Inline
Process Connection Location:	Lower, top, left or right side
Case Enclosure Rating:	Weatherproof, IP65
Fill Fluid:	Glycerine standard, Food grade silicone (XCZ), Food grade mineral oil (XMY)(4)
Seal Surface Finish:	12-20Ra
Display Type:	Full 5 digital LCD
Backlight:	Optional, (battery Backup required on 213X loop powered)
Bar Graph:	10 Segment
Battery Life:	450 hrs., Battery life indicator (STD.)
Configuration Mode:	Allows for changes to default settings of gauge Including password, zero disable, recalibration, restore factory defaults
Switch Setpoint	Program and switch setpoints
Update Rate	100 ms, 200 ms, 500 ms, 1 sec
Dampening	None, average, 2, 4, 6, 8 times per 100ms

WETTED COMPONENTS

Model	Diaphragm	Seal Housing	Joints
2030	316L SS electopolished	316L SS	Welded

NON-WETTED COMPONENTS

Model	Case
2030 Sanitary	304 SS, Electro Polished/Tumbled

MIN/MAX TEMPERATURE LIMITS

Ambient	Process	Storage
14°F to 140°F (–10°C to 60°C)	14°F to 275°F (–10°C to 135°C)	–4°F to 158°F (–20°C to 70°C)

AGENCY APPROVALS

3A Sanitary
Material Traceability Certification to EN 10204: 2004 3.1 standard
ASME B40.7

2030
3" dial size